Microstructure and Mechanical Properties of Friction Stir Welded Kanthal APMT™

A Thesis

Presented in Partial Fulfillment of the Requirements for the

Degree of Master of Science

with a

Major in Metallurgical Engineering

in the

College of Graduate Studies

University of Idaho

by

Anumat Sittiho

Major Professor: Indrajit Charit, Ph.D.

Committee Members: Krishnan Raja, Ph.D., Samrat Choudhury, Ph.D.

Department Administrator: D. Eric Aston, Ph.D.

August 2017

Authorization to Submit Thesis

This thesis of Anumat Sittiho, submitted for the degree of Master of Science with a major in Metallurgical Engineering and titled "Microstructure and Mechanical Properties of Friction Stir Welded Kanthal APMT^{TM}," has been reviewed in final form. Permission, as indicated by the signatures and dates below, is now granted to submit final copies to the College of Graduate Studies for approval.

Major Professor: _____ Date: _____

Indrajit Charit, Ph.D.

Committee Members: _____ Date: _____

Krishnan Raja, Ph.D.

_____ Date: _____

Samrat Choudhury, Ph.D.

Department Administrator: _____ Date: _____

D. Eric Aston, Ph.D.

Abstract

Commercial Kanthal APMT^{TM} steel (Fe-22Cr-5Al-3Mo) was developed for use as high-temperature furnace elements. The alloy is not considered to have good weldability because of various metallurgical issues. Friction stir welding (FSW) was applied to a Kanthal APMT^{TM} plate in a bead-on-plate configuration using a PCBN tool with a tool rotation rate of 600 RPM and a traverse speed of 25.4 mm/min. Microstructure and mechanical properties were evaluated to determine the weld quality and to examine the feasibility of applying FSW as a joining/processing technique. Microstructural characteristics were mainly studied both by optical and electron microscopy. The stir zone contains small equiaxed grain structure. Interestingly, Vickers microhardness profile across the processed zone has revealed no significant change in microhardness. Thermal stability of the alloy at 475 ^{o}C is also studied. The results show that FSW slows down the embrittlement effect but does not entirely stop it.

Acknowledgement

It is my great pleasure to express my deep sense of gratitude to my academic advisor, Dr. Indrajit Charit, for his keen attention, constant encouragement and inspiring guidance without which this work would not have come to success. I am grateful to my committee member, Dr. Krishnan Raja and Dr. Samrat Choudhury, for their insight and support.

I would like to thank several other people, such as, Dr. Vedavyas Tungala, Dr. Rajiv Mishra, Aniket Kumar Dutt (University of the North Texas), Dr. Thomas Williams (University of Idaho) for help and suggestion. Also, Special thanks to my lab colleagues, Cody, Ankan, Martin, Arnab, Dallas, for their assistance, support and friendship.

The material used in this work was procured by using funds by the Nuclear Energy University Programs (NEUP). Also, Anumat Sittiho would like to acknowledge The Royal Thai Navy for providing me a scholarship during his graduate studies at the University of Idaho.

Finally, thanks and acknowledgements go to everyone without whom I could not have reached where I am right now.

Dedication

"*Behind an able man there are always other able men*."

Anonymous.

This work is dedicated to my wife, Siriporn, son, Galin, and my parents.

Table of Contents

List of Tables

List of Figures

Chapter 1: Introduction

1.1 Background

One of the most prominent challenges in Material Science and Engineering in the last century is to expand the materials usage to withstand the ever more severe service condition such as higher operating temperature and harsh corrosive environments within reasonable costs. One of the big leap in steel making process has been the use of powder metallurgy to produce steels. However, powder metallurgy steels have certain inherent issues in that they are difficult to join via fusion welding because of there are melting and solidification involve. Friction stir welding (FSW), a solid-state welding technique, was developed by The Welding Institute (TWI), Cambridge, UK [1]. This technique was initially applied to aluminum alloys [1]. Nowadays, FSW has become a promising joining technique for a wide array of metallic alloys including aluminum alloys, magnesium alloys, titanium alloys, nickel based superalloys as well as steels [1-18].

Kanthal APMT^{TM} is a high chromium aluminum bearing dispersion-strengthened ferritic stainless steel that is made by powder metallurgy techniques including rapid solidification (RSP) and hot isostatic pressing (HIP). The production route of APMT^{TM} steel is shown in Figure 1.1 [19]. The production route is currently applied for Kanthal APM and Kanthal APMT^{TM}. The RSP step offers several advantages over conventional casting processes as listed below [20]:

1. An extension of solid solubility, often by orders of magnitude;

2. Enhanced compositional flexibility;

3. Formation of non-equilibrium or metastable crystalline phases from the melt through alternate phase selection processes and/or an incorporation of desirable second-phases like fine dispersoids and ductile particles;

4. A reduction in both the number and size of segregated phases;

5. Retention of disordered crystalline structure in normally ordered materials and intermetallic compounds;

6. The intrinsic microstructural effects include either one or a combination of changes in grain morphology, refinement of features, such as the size and shape of grains, and the shape and location of the phases present.

Therefore, alloys produced by this method have generally better mechanical properties than conventional production route FeCrAl alloys. The advantage of FeCrAl over other stainless steels is the presence of stable impervious protective film of α-alumina (Al_2O_3). The film grows slowly and can withstand the temperature up to 1400 ^oC while the conventional chromia film (Cr_2O_3) is stable up to 1100 ^oC [19, 21]. Presence of minor elements such as Y and Hf improve the oxidation resistance of these alumina forming alloy [22-24]. Nevertheless, conventional FeCrAl alloys have low mechanical properties. Kanthal APM (Fe-5.8%Al-22.0%Cr) was developed to have improved mechanical properties over the conventional FeCrAl alloys by means of solid solution strengthening, dispersion strengthening and applying powder metallurgy in the production route. Kanthal APMT^{TM} is further increased the high temperature mechanical properties over Kanthal APM by adding Mo which imparts solid solution strengthening effect. Figure 1.2 compares the operating window of chromia forming and alumina forming alloys [19]. Kanthal APMT^{TM} contains dispersed particles homogeneously distribute in the alloy matrix and relatively large grain size (40-110 μm) depending on the product forms and processing details. These microstructural features are beneficial for high temperature mechanical properties. Kanthal APMT^{TM} is designed for high temperature application purposed, such as furnace furniture and thermocouple protecting tube. Nonetheless, presence of particles can also act as the defects sinks under irradiation [25]. Because of these properties, Kanthal APMT^{TM} is being investigated as substitute for the zirconium alloy based nuclear fuel rod [21,26-27].

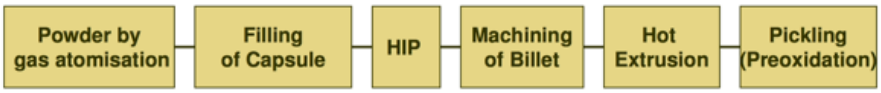

Figure 1.1. Production process procedure for making Kanthal APMT^{TM} [19].

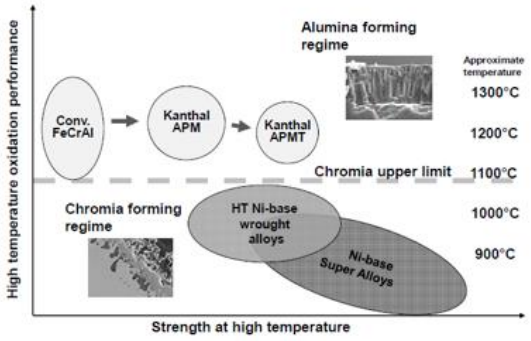

Figure 1.2. Operating windows of high temperature protection film [19].

Despite the fact that powder metallurgy FeCrAl alloys can tolerate high temperature working environment, they have inherent the difficulties in being welded through the conventional means. Applying traditional fusion welding poses problems to alloys, such as phase segregation and chemical heterogeneity, disturbance of powder metallurgy structure, weld cracking, type iv cracking, wide heat affected zone (HAZ) etc. [26, 28-32]. However, there is a possible way out by utilizing a solid-state welding technique.

1.2 Metallurgy of steel welding

The definition of welding is: "Welding is a process in which materials of the same fundamental type or class are brought together and caused to join (and become one) through the formation of primary (and, occasionally, secondary) chemical bonds under the combined action of heat and pressure" [33]. In the early age of human civilization, people used to create joint materials by hammer welding and riveting. The fusion welding was invented after the discovery of acetylene gas and battery electrode in early 19^{th} century. From that time on, fusion welding has become a widely-used method for joining steels and used widely till date. During the fusion welding process, the materials undergo both the melting and solidification process and dissipate the heat throughout the vicinity area. This thermal cycle can be divided into three regimes, namely, weld zone, heat affected zone, and base metal. In the weld zone, the metal receives heat from the welding electrode and undergoes melting and solidification. The HAZ is the region where the grain structure is exposed to the heat from the process. However, the heat is not enough for melting the metals but can affect the mechanical properties and microstructure of the workpiece. Base metal is where the metals is not affected by the welding process.

Detrimental effects from fusion welding on high chromium ferritic stainless steels are from phase transformations (changing in microstructures by phase transformation), high residual stresses, or deterioration of second phase precipitates by heat. To predict phase transformation in ferritic stainless steel, we can use a Fe-Cr binary phase diagram or ternary phase diagram such as Fe-Cr-Al system. During thermal cycle of welding, if the cooling rate is fast enough austenite can transform into martensite, which reduces the toughness of steels. Martensitic phase can be predicted by using composition of steels and Schaeffler diagram in

Figure 1.3 [34]. Detrimental phases that cause the embrittlement during the welding process in stainless steel are alpha prime (α'), sigma (σ), chi (χ) phases and constituent particles [35].

Sigma (σ) phase is a non-magnetic intermetallic phase composed mainly of iron and chromium which forms in ferritic and austenitic stainless steels during exposure at 560 ºC to 815 ºC. Fortunately, the kinetics of σ phase formation is slow in ferritic steel so there is not much problem from this phase in welding [36].

Chi (χ) phase is related to σ phase. It occurs at 550-990 ºC. The χ-phase, having composition Fe_2CrMo, can be found in ferritic steel bearing molybdenum. The effects of χ phase in ferritic steels are lowering notch toughness accompanied with decrease in ductility. In prolonged aging, χ phase transforms into σ phase.

Alpha prime (α') phase (the reason for 475 ºC embrittlement) is chromium-rich precipitates. It drastically reduces toughness of ferritic steels. It also raises DBTT, thus affecting the room temperature toughness, too. Using optical metallography cannot distinguish this phase. High chromium alloys are more susceptible by this deteriorative phenomenon. Details of 475 ºC embrittlement will be discussed later.

Other phases that can form in such steels include such as $Cr_{23}C_6$, $FeAl_3$, Al_4C_3 and so forth Fe-Al intermetallic forms when concentration of Al is more than 15 at% [37]. These intermetallic phases are FeAl and Fe_3Al which are brittle phases and might cause problem to the system [38]. The amount of $Cr_{23}C_6$ can be minimized by alloying the steel with elements such as Ti and Nb to capture C and N in the alloys. Thus, Cr concentration is not affected.

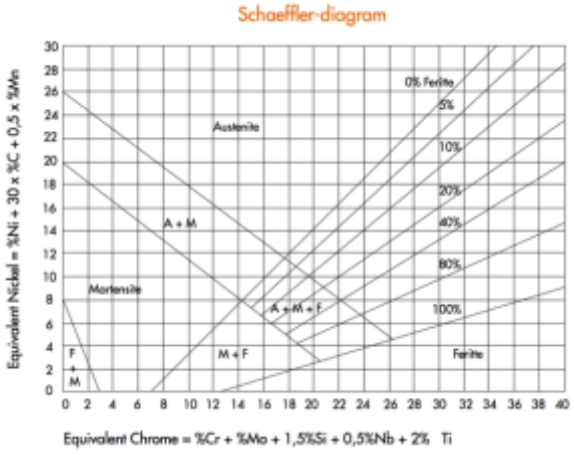

Figure 1.3. Schaeffler diagram with:

• Cr equivalent = (Cr)+2(Si)+1.5(Mo)+5(V)+5.5(Al)+1.75(Nb)+1.5(Ti)+0.75(W)

• Ni equivalent = (Ni)+(Co)+0.5(Mn)+0.3(Cu)+25(N)+30(C) [34].

1.3 Solid-state welding

Solid-state welding is a welding technique that does not involve the melting. Solid-state welding techniques up to present time are hammer welding, resistance welding, high-frequency welding, friction welding, explosion welding, ultrasonic welding, diffusion welding, and friction stir welding [39-44]. These solid-state welding techniques find themselves in very useful applications such as joining the dissimilar metals or alloys, very small area joining, high weld efficiency, affiliating sandwich structure. Some of the solid-state weldings will be discussed in brief within in the following sections.

1.3.1 Explosive welding

Explosive welding is the solid-state welding technique that is used mainly in the plate structure. The method of the weld involves putting two surface-cleaned metal on the top of each other. The top plate is then layered with the explosive compound. The detonation from the explosion drives the plate to contact with another at high speed and the bonding between the plate occurs. The importance of explosion welding is its ability to join quite dissimilar metals such as aluminum or titanium to steel [39].

1.3.2 Diffusion welding

Diffusion welding involves coupling specimens together with heat applied and wait for the diffusion to take place across the interface between the two materials. Diffusion welding is based mainly on the kinetics of diffusion of elements, thereby, depending on temperature exponentially. This welding method usually takes longer time and thus limit the productivity of the technique [40]. This technique shows promising mechanical properties in the result because the heat during the welding is homogenous over the bulk materials. Also, it can be used to join different metals [41].

1.3.3 Friction welding

The method of joining two parts together by using heat from the friction and applying force between two specimens. This method proof itself of the capability for joining two similar or dissimilar metal pieces. The limit of the technique is in the specimen geometry and the size of the specimen. Since the welding parameters require the specific shape and size of materials, friction welding has some restriction for the fabrication of alloys.

1.3.4 Ultrasonic welding

Similar to friction welding, ultrasonic welding uses the mean of rubbing two specimens to create a weld. This welding technique involves coupling two materials under the sonotrode tips and passes the ultrasonic wave parallel to the weld (perpendicular to the forging direction of the tip). The factors that govern the successful ultrasonic welding are the optimum combination of pressing force, oscillation speed and duration of holding. The technique is reported to be applicable to various types of different metallic alloys [42], plastics [43] and textile materials [44].

1.4 Objectives of the present study

The purpose of this work is to evaluate the applicability of friction stir welding technique with the Kanthal APMT^{TM} plate and study in detail the benefits and disadvantages of applying this joining method. The mechanical testing in this work involves Vickers microhardness testing and tensile testing at room temperature. Microstructural characteristics are studied by optical microscopy, scanning and transmission electron microscopy. Hence, the thesis aims to evaluate the feasibility of applying FSW for joining Kanthal APMT^{TM} and similar types of alloys. The thermal stability of the as received alloy and FSWed specimen are also studied with a focus on the 475 ^{o}C embrittlement phenomenon.

References

1. Thomas, W. M., Nicolas, E. D., Needham, J. C., Murch, M. G., Temple-Smith, P., & Dawes, C. J. (1995). *U.S. Patent No. 5460317*. Washington, DC: U.S. Patent and Trademark Office. Friction Welding.

2. Buhl, N., Wagner, G., Eifler, D., Gutensohn, M., & Zillekens, F. (2013). Microstructural and Mechanical Investigations of Friction Stir Welded TI/TI-And TI-Alloy/TI-Alloy-Joints. In *Friction Stir Welding and Processing VII* (pp. 141-149). Springer International Publishing.

3. Sutton, M. A., Yang, B., Reynolds, A. P., & Taylor, R. (2002). Microstructural studies of friction stir welds in 2024-T3 aluminum. *Materials Science and Engineering: A*, *323*(1), 160-166.

4. Jata, K. V., Sankaran, K. K., & Ruschau, J. J. (2000). Friction-stir welding effects on microstructure and fatigue of aluminum alloy 7050-T7451. *Metallurgical and Materials Transactions A*, *31*(9), 2181-2192.

5. Liu, G., Murr, L. E., Niou, C. S., McClure, J. C., & Vega, F. R. (1997). Microstructural aspects of the friction-stir welding of 6061-T6 aluminum. *Scripta Materialia*, *37*(3), 355-361.

6. Rhodes, C. G., Mahoney, M. W., Bingel, W. H., Spurling, R. A., & Bampton, C. C. (1997). Effects of friction stir welding on microstructure of 7075 aluminum. *Scripta Materialia*, *36*(1), 69-75.

7. Esparza, J. A., Davis, W. C., Trillo, E. A., & Murr, L. E. (2002). Friction-stir welding of magnesium alloy AZ31B. *Journal of Materials Science Letters*, *21*(12), 917-920.

8. Ye, F., Fujii, H., Tsumura, T., & Nakata, K. (2006). Friction stir welding of Inconel alloy 600. *Journal of Materials Science*, *41*(16), 5376-5379.

9. Chen, Y. C., Fujii, H., Tsumura, T., Kitagawa, Y., Nakata, K., Ikeuchi, K. et al. (2009). Friction stir processing of 316L stainless steel plate. *Science and Technology of Welding and Joining*, *14*(3), 197-201.

10. Allart, M., Benoit, A., Paillard, P., Rückert, G., & Chargy, M. (2014). Metallurgical study of friction stir welded high strength steels for shipbuilding. *Materials Science Forum*, *783-786*, 2798-2803.

11. Xue, P., Ma, Z. Y., Komizo, Y., & Fujii, H. (2016). Achieving ultrafine-grained ferrite structure in friction stir processed weld metal. *Materials Letters*, *162*, 161-164.

12. Sabooni, S., Karimzadeh, F., Enayati, M. H., & Ngan, A. H. W. (2015). Friction-stir welding of ultrafine grained austenitic 304L stainless steel produced by martensitic thermomechanical processing. *Materials & Design*, *76*, 130-140.

13. Baker, B. W., Menon, E. S. K., McNelley, T. R., Brewer, L. N., El-Dasher, B., Farmer, J. C., & Sanderson, S. (2014). Processing-microstructure relationships in friction stir welding of MA956 oxide dispersion strengthened steel. *Metallurgical and Materials Transactions E*, *1*(4), 318-330.

14. Noh, S., Kasada, R., Kimura, A., Park, S. H. C., & Hirano, S. (2011). Microstructure and mechanical properties of friction stir processed ODS ferritic steels. *Journal of Nuclear Materials*, *417*(1), 245-248.

15. Wang, J., Yuan, W., Mishra, R. S., & Charit, I. (2013). Microstructural evolution and mechanical properties of friction stir welded ODS alloy MA754. *Journal of Nuclear Materials*, *442*(1), 1-6.

16. Han, W., Chen, D., Ha, Y., Kimura, A., Serizawa, H., Fujii, H., & Morisada, Y. (2015). Modifications of grain-boundary structure by friction stir welding in the joint of nano-structured oxide dispersion strengthened ferritic steel and reduced activation martensitic steel. *Scripta Materialia*, *105*, 2-5.

17. Mathon, M. H., Klosek, V., De Carlan, Y., & Forest, L. (2009). Study of PM2000 microstructure evolution following FSW process. *Journal of Nuclear Materials*, *386*, 475-478.

18. Ma, Z. Y., Xiao, B. L., Yang, J., & Feng, A. H. (2010). Friction stir processing: a novel approach for microstructure refinement of magnesium alloys. In *Materials Science Forum* (Vol. 638, pp. 1191-1196). Trans Tech Publications.

19. Jönsson, B., Lu, Q., Chandrasekaran, D., Berglund, R., & Rave, F. (2013). Oxidation and Creep Limited Lifetime of Kanthal APMT™, a Dispersion Strengthened FeCrAlMo Alloy Designed for Strength and Oxidation Resistance at High Temperatures. *Oxidation of metals*, *79*(1-2), 29-39.

20. Lavernia, E. J., & Srivatsan, T. S. (2010). The rapid solidification processing of materials: science, principles, technology, advances, and applications. *Journal of Materials Science*, *45*(2), 287.

21. Yamamoto, Y., Pint, B. A., Terrani, K. A., Field, K. G., Yang, Y., & Snead, L. L. (2015). Development and property evaluation of nuclear grade wrought FeCrAl fuel cladding for light water reactors. *Journal of Nuclear Materials*, *467*, 703-716.

22. Unocic, K. A., Yamamoto, Y., & Pint, B. A. (2017). Effect of Al and Cr content on air and steam oxidation of FeCrAl alloys and commercial APMT alloy. *Oxidation of Metals*, *87*(3-4), 431-441.

23. Kochubey, V., Al-Badairy, H., Tatlock, G., Le-Coze, J., Naumenko, D., & Quadakkers, W. J. (2005). Effects of minor additions and impurities on oxidation behavior of FeCrAl alloys. Development of novel surface coatings compositions. *Materials and Corrosion*, *56*(12), 848-853.

24. Pint, B. A. (2003). Optimization of reactive-element additions to improve oxidation performance of alumina-forming alloys. *Journal of the American Ceramic Society*, *86*(4), 686-695.

25. De Castro, V., Briceno, M., Jenkins, M. L., Kirk, M., Lozano-Perez, S., & Roberts, S. G. (2014). In-situ Fe+ ion irradiation of an oxide dispersion strengthened steel. In: *Journal of Physics: Conference Series*, 522(1), 012032.

26. Field, K. G., Gussev, M. N., Yamamoto, Y., & Snead, L. L. (2014). Deformation behavior of laser welds in high temperature oxidation resistant Fe–Cr–Al alloys for fuel cladding applications. *Journal of Nuclear Materials*, *454*(1), 352-358.

27. Pint, B. A., Terrani, K. A., Brady, M. P., Cheng, T., & Keiser, J. R. (2013). High temperature oxidation of fuel cladding candidate materials in steam–hydrogen environments. *Journal of Nuclear Materials*, *440*(1), 420-427.

28. Regina, J. R., Dupont, J. N., & Marder, A. R. (2007). The effect of chromium on the weldability and microstructure of Fe-Cr-Al weld cladding. Welding Journal, *86*(6), 170.

29. Boegelein, T., Dryepondt, S. N., Pandey, A., Dawson, K., & Tatlock, G. J. (2015). Mechanical response and deformation mechanisms of ferritic oxide dispersion strengthened steel structures produced by selective laser melting. *Acta Materialia*, *87*, 201-215.

30. *FAQ: What is type IV cracking, and how is it detected?*. (2017). *Twi-global.com*. Retrieved 16th May 2017, from http://www.twi-global.com/technical-knowledge/faqs/material-faqs/faq-what-is-type-iv-cracking-and-how-is-it-detected/

31. Francis, J. A., Mazur, W., & Bhadeshia, H. K. D. H. (2006). Review type IV cracking in ferritic power plant steels. *Materials Science and Technology*, *22*(12), 1387-1395.

32. Gussev, M. N., Field, K. G., & Yamamoto, Y. (2017). Design, properties, and weldability of advanced oxidation-resistant FeCrAl alloys. *Materials & Design*, *129*, 227-238.

33. Messler, R. (1999). *Principles of Welding* (1st ed., pp. 3). New York: John Wiley.

34. *Dacapo.com*. Retrieved 26th December 2016, from http://dacapo.com/uploads/documents/40-document.pdf

35. Bhadeshia, H. & Honeycombe, R. (2011). *Steels: Microstructure and Properties* (3rd ed., pp. 260). Amsterdam: Elsevier, Butterworth-Heinemann.

36. Hsieh, C. C., & Wu, W. (2012). Overview of Intermetallic Sigma (σ) Phase Precipitation in Stainless Steels. *ISRN Metallurgy, 2012* (http://dx.doi.org/10.5402/2012/732471).

37. Palm, M. (2005). Concepts derived from phase diagram studies for the strengthening of Fe–Al-based alloys. *Intermetallics*, *13*(12), 1286-1295.

38. Kim, S. H., Kim, H., & Kim, N. J. (2015). Brittle intermetallic compound makes ultrastrong low-density steel with large ductility. *Nature*, *518*(7537), 77-79.

39. Linse, V. D., & Lalwaney, N. S. (1984). Explosive welding. *JOM*, *36*(5), 62-65

40. Owczarski, W. (1981). Application of diffusion welding in the U.S. *Welding Journal*, *60*(2), 22-33.

41. Akca, E., & Gursel, A. (2017). The effect of diffusion welding parameters on the Mechanical Properties of Titanium Alloy and Aluminum Couples. *Metals*, *7*(1), 22.

42. Matsuoka, S. I., & Imai, H. (2009). Direct welding of different metals used ultrasonic vibration. *Journal of Materials Processing Technology*, *209*(2), 954-960.

43. Zhang, Z., Wang, X., Luo, Y., Zhang, Z., & Wang, L. (2010). Study on heating process of ultrasonic welding for thermoplastics. *Journal of Thermoplastic Composite Materials*, *23*(5), 647-664.

44. Shi, W., & Little, T. (2000). Mechanisms of ultrasonic joining of textile materials. *International Journal of Clothing Science and Technology*, *12*(5), 331-350.

Chapter 2: Literature Survey

Friction stir welding (FSW) is a solid-state welding technique invented by The Welding Institute (TWI), Cambridge, UK in 1994. First, the technique was applied to aluminum and magnesium alloys. Later, FSW is used to apply to other types of metallic alloys and has since become very widely explored topic of active research. In FSW, there is no melting-solidification involved so that it gives several benefits such as joining different metallic alloys, joining unweldable alloys or even can repair fusion welds. This chapter will be focused on the FSW process, procedures, and overview of relevant FSW research in steels.

2.1 Friction stir welding process and parameters

The process of friction stir welding (FSW) involves plunging the non-consumable tools into the workpiece. The tool is then rotated at high speed and moved along the weld direction. A schematic of overall FSW process is shown in Figure 2.1(a). The FSW process is influenced by heat and flow of materials during the process. The process has different parameters such as welding tool features, welding parameters, and weld design. The effects of thermal and mechanical cycle during the FSW process create four distinctive regimes across the transverse direction of the weld. Figure 2.1(b) shows a transverse cross section of a friction stir welded aluminum alloy showing main distinct regions (the base material region is not shown in the figure). Those four regions can be described as follows:

1. Stir zone (SZ) or nugget

Stir zone is the area where the material is directly affected by the tool pin and shoulder. The processed materials are subjected to intensive deformation and receive high temperature created by the friction between the tool shoulder and the workpiece surface and adiabatic heating arising out of high strain rate severe plastic deformation. The material movement during FSW is sometimes likened with hot extrusion. During the process, the material undergoes dynamic recrystallization (DRX) and some level of grain growth by the effect of the heat at the back of the leaving tool. Fine equiaxed grain structure is the characteristic of the SZ.

2. Thermomechanically affected zone (TMAZ)

Adjacent to the SZ is TMAZ. Tool/material interaction influences TMAZ final microstructure. Recrystallization is not readily apparent in TMAZ but heavily distorted grain

structure is generally observed. However, the extent of deformation and temperature are not high enough to create the DRX. Thus, the microstructure features in TMAZ include severely distorted grains which align themselves along the flow of the material during FSW. Some different features from the interface of SZ/TMAZ can be seen in optical micrograph that the interface on the advancing side is more distinguished than that on the retreating side.

3. Heat affected zone (HAZ)

Heat affected zone is further away from TMAZ. Thus, it is only affected by thermal cycles during FSW. Generally, the overall grain morphology appears the same as the base metal but the mechanical properties may alter due to the effects of thermal cycles and induced fine microstructural changes (precipitate coarsening, grain growth, etc.).

4. *Base metal (BM)*

This regime is not affected by either thermal or mechanical effects from the process. Hence, the mechanical properties and microstructures are retained.

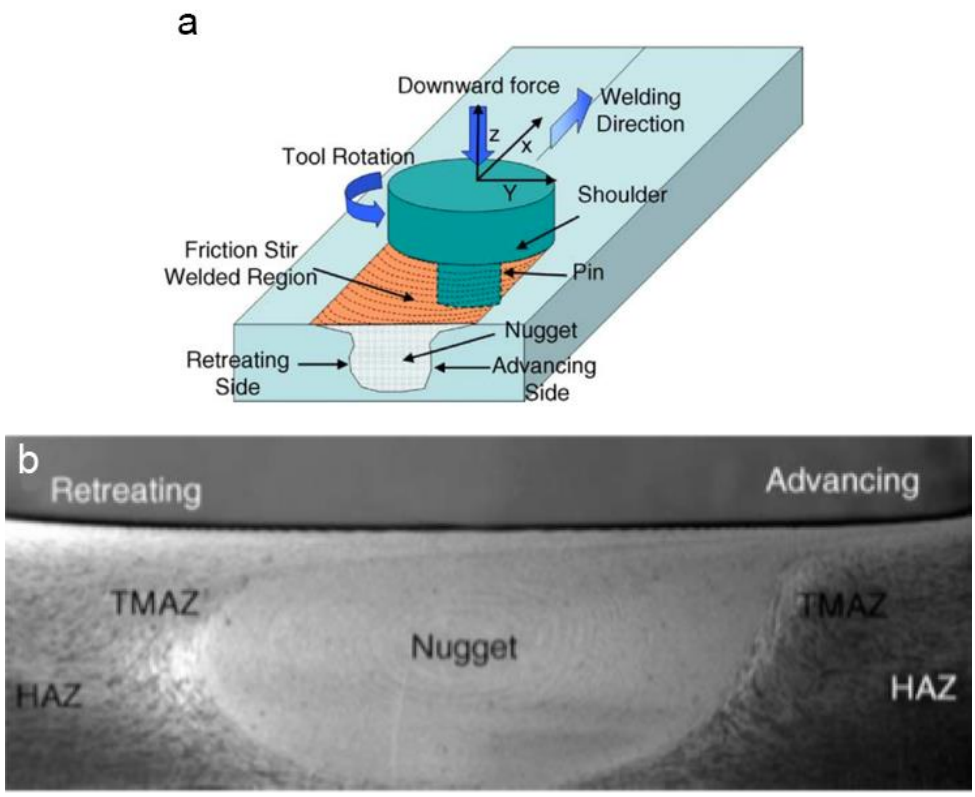

Figure 2.1. a) Schematic of FSW and terminology and b) Typical microstructure from transverse cross section in FSW of metal alloys [1].

2.2 FSW tooling

FSW tooling is typically made of high temperature and high strength materials. A tool comprises of a tool shoulder and a pin underneath the shoulder, as shown in Figure 2.1 (a). The function of the tool shoulder is mainly generating the friction force between the rotational movement of the tool and the surface of the substrate materials. The pin moves the viscous material from the front to the back, which gets consolidated under the action of the tool shoulder. Tool materials selected include tool steels, ceramic materials, and tungsten based material depending on the characteristics of materials to be welded [2]. For aluminum alloys FSW, the tool steel will usually be a material of choice because it provides enough strength at the process temperature. In steel and high temperature alloys e.g. titanium alloys, the tools are generally made of polycrystalline cubic boron nitride (PCBN) or W-based materials such as W-Re or WC-Co cermet. PCBN is among the hardest material after the diamond [3]. Its combination of good hardness and toughness makes it very attractive in tooling application in metallurgy. The materials chosen for FSW tooling must be able to maintain the mechanical integrity at high temperature during the process to retain the shape and commence welding the materials without tools failure.

By understanding the mechanisms of the flow of material involved and heat generation during FSW, a FSW tool can be designed to have higher efficiency. The shoulder of the spindle plays a significant role in the generation of heat, by which the material is plasticized, and keeps the welded materials confined in the location [4]. Flat shoulder profile is not good in entrapping the materials and tend to create a lot of metal flash during FSW. Some tool configuration designs and maximum joining thickness are shown in Figure 2.2-Figure 2.4.

A pin profile determines the rate of swept volume of material in the weld [1]. In FSW of thick plates, a pin also serves as the additional heat generator to the process. The length of the pin can affect the maximum welding speed because the excess load exerted to the pin may fail it. TWI has developed various types of FSW tool pins for using in different thickness of the workpieces and configuration of joints. The conventional cylindrical threaded pin probe is adequate for butt welding of aluminum based material plates of thickness up to ~12 mm. When welding thicker plate, the Whorl^{TM} and MX-Triflute^{TM} should be used [5]. In lap joint weld configurations, FSW typically creates a thinning defect on the retreating side of the weld as shown in Figure 2.5. Developed tool types for lap joint welding are Flared-Triflute^{TM} and Skew-

Stir™, shown in Figure 2.6 (a) and (b). Rotary skew-stir tooling makes wider SZ because of the oblique axis of the probe and the rotational axis. This tool feature was reported to help reduce the void defect of the weld by 30% [6]. New tool development could be the driver for incorporating further innovation in the FSW process such as enabling it to the portable welding [7]. FSW process needs the anvil plate to support the weld workpieces. With bobbin FSW tool, illustrated in Figure 2.6 (c), the anvil is substituted by another tool shoulder clamping the workpiece in the middle. Bobbin FSW tool has been shown to be effective for joining hollow extrusions and lap joints [7].

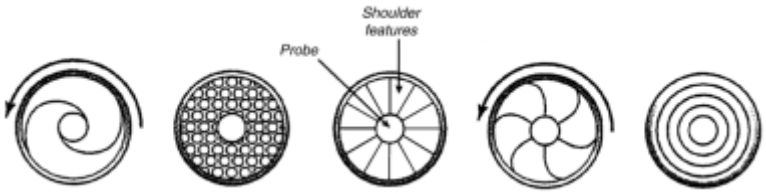

Figure 2.2 Different type of FSW tool shoulder profiles [1].

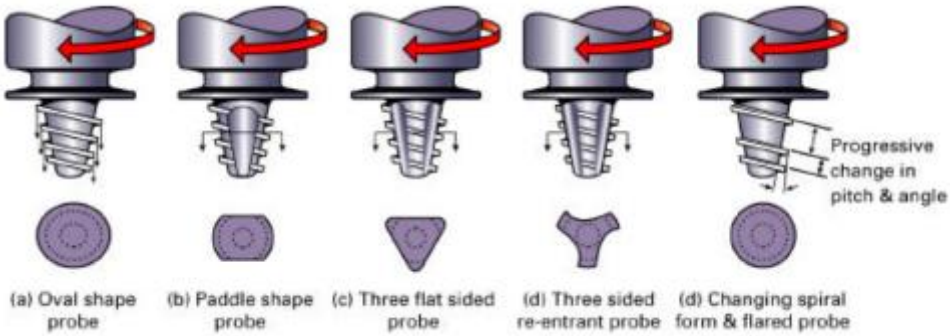

Figure 2.3. Various FSW pin types for welding a butt joint [5].

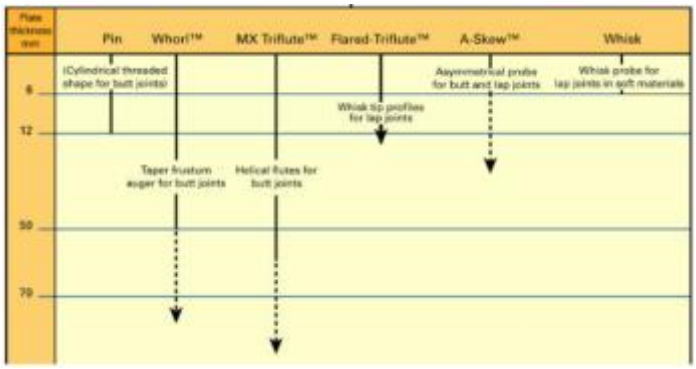

Figure 2.4. Different tool shoulder types with maximum welding thickness in butt joint welding [5].

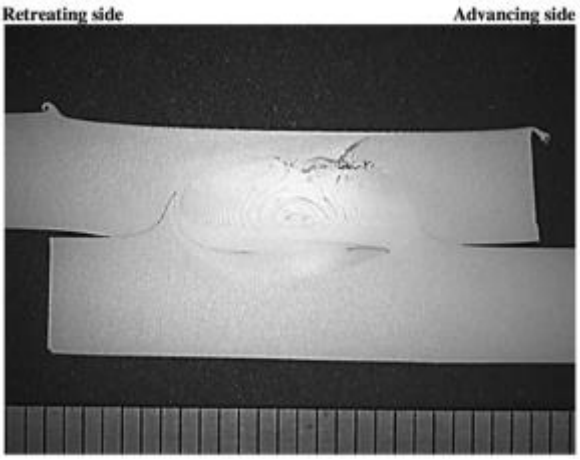

Figure 2.5. Thinning defect when using pin type tool [8].

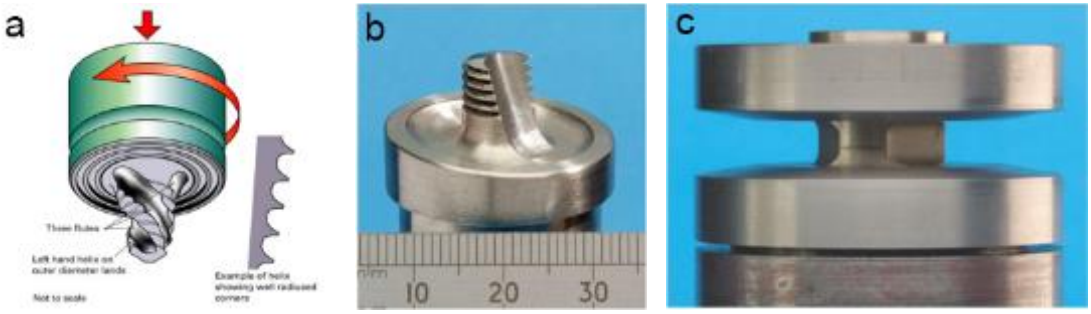

Figure 2.6. (a) MX-Triflute^{TM} probe and [9] (b) Skew-stir^{TM} probe (Copyright © 2001, TWI Ltd) [6] and (c) FSW bobbin tool [7].

2.3 Heat generation and mass flow during FSW

During the processing of metals, the critical parameters that an engineer needs to learn are the heat that added into the metals and how the workpieces behave under such circumstance. Unlike other metallurgical process where heat input can be controlled by using a heating coil or a furnace, complex heat generation in FSW comes from the friction of tool shoulder/specimen surface and adiabatic deformation of a workpiece. In FSW, the welding parameters i.e. tools design features, forging force, rotational speed and traverse speed can alter the formation of material flow and heat input in the FSW workpieces. Because of the complexity of the process, experimental analysis of these parameters is rather difficult. Attempts to measure the temperature of the process was done by inserting the thermocouples into the workpiece at different positions closed to the weld zone [10-12]. Using this method,

the temperature is obtained but the thermocouples are destroyed. Recently, advent of computer simulation works well for solving the problems [12-21].

Metals movement in FSW can be treated as a hot extrusion process where the material is softened and extruded through the confined area between the tool and the colder area of the material around the periphery. Hence, the behavior of the metal flow behaves like one under thermo-mechanical process. The strain rate of FSW can be as much as 150 s^{-1} [13] or 1000 s^{-1} [14]. There are two methods used for studying the flow of materials during FSW i.e. computer simulation and marker insert technique (MIT). In MIT, the traceable dissimilar particles are embedded in the materials prior to the process. After the materials undergo FSW, the markers are observed for their changed location. Seidel and Reynolds [11] studied the actual flow of materials during FSW by using MIT. Figure 2.7 (a) shows the pattern of the flow that material is cut from the front of the advancing side and the front of the tool. Then it is transferred around the tools and extruded through the retreating side and escaped at the back of the tools. Meanwhile, some parts of the metal are transferred back to the advancing side and fill the first shear gap. The effect of the pin is that the metal is pushed down near the pin contact in the advancing side and circulated up at the retreating side of the weld as shown in Figure 2.7 (b) and (c). This flow cause the distinct microstructure pattern called 'onion ring' pattern in some metals during FSW.

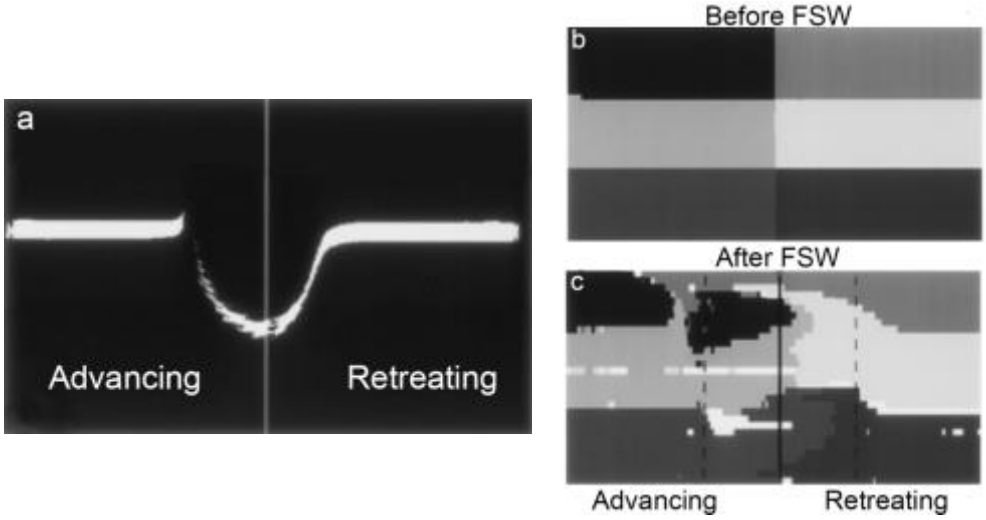

Figure 2.7. Material flow during FSW using MIT technique from: (a) normal direction of the weld, (b) and (c) transverse direction of the weld [11].

In computational technique, the material flow is considered as non-Newtonian viscous fluid flow. The flow of materials is then computerized base on the fluid mechanics principles [15, 16]. The 2D viscosity of materials, μ, can be described as a function of strain rate and temperature [17], which can be written as

$$\mu = \frac{\sigma_f}{3\dot{\varepsilon}} \qquad (2.1)$$

where the strain rate, $\dot{\varepsilon}$, is the combination of plane strain tensor; ε_{ij} and σ_f is flow stress.

$$\dot{\varepsilon} = \left(\frac{2}{3}\varepsilon_{ij}\varepsilon_{ij}\right)^{1/2} \qquad (2.2)$$

$$\varepsilon_{ij} = \frac{1}{2}\left(\frac{\partial u_i}{\partial x_j} + \frac{\partial u_j}{\partial x_i}\right) \qquad (2.3)$$

The term flow stress, σ_f, can be determined by using Zener-Hollomon parameter. Given that *A*, α, and *n* are material constants, then

$$Z = \dot{\varepsilon} exp(\frac{Q}{RT}) \qquad (2.4)$$

$$\sigma_f = \frac{1}{\alpha} sinh^{-1}\left[\left(\frac{Z}{A}\right)^{\frac{1}{n}}\right] \qquad (2.5).$$

When the Equation 2.1-2.5 are solved, the result shows that the viscosity will be lower at higher temperature and higher strain rate and vice versa, as shown in the plot of Figure 2.8. The strain rate is highest near the tool pin and shoulder, and is lower as the observed area move out of the influence of the tool.

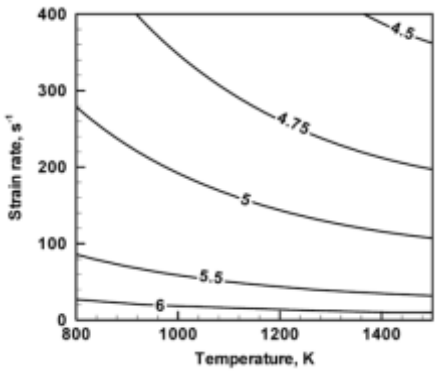

Figure 2.8. Viscosity contour in the temperature and strain rate space [13].

While considering the behavior of metals during FSW, they are treated as non-Newtonian incompressible fluid [12, 13]. Work by Smith [12] suggested that at the initial state

(plunging), the major contribution of heat is from friction between tool and workpiece. However, during the process, the heat source is solely from the viscous dissipation of mechanical energy. Colegrove *et al.* [19] also modeled the FSW heat and mass transfer in aluminum alloys and concluded that the heat generated by viscous dissipation is good enough to describe the associated thermal energy of the process. Zhu *et al.* [18] used finite element analysis to calculate the heat generated in FSW of 304L stainless steel by considering that the heat is generated by the friction between tool/specimen and thermal stress. The calculated temperature and experimental temperature results were different (up to 25%) but had the same changing trend. Nandan *et al.* [13] studied the FSW in mild steel (1018 stainless steel) and found that the heat generated in FSW is created by both friction between tool/specimen and viscous dissipation. The portions of heat are divided by slip factor; δ, in which the slipping and sticking portion of a metal under FSW are divided (δ=1 means fully sticking condition).

Heat transfer in FSW process can by determined by thinking about the workpiece as incompressible non-Newtonian viscous fluid with the moving heat source. From this assumption, the thermal model can be described by using energy conservation equation proposed by Nandan *et al.* [13]. Conservation of mass in incompressible fluid yield the simple equation of;

$$\frac{\partial U_i}{\partial x_i} = 0 \,, \qquad (2.6)$$

conservation of momentum lead to equation;

$$\frac{\partial \sigma_i}{\partial x_i} = 0 \,, \qquad (2.7)$$

and conservation of energy;

$$\rho C_p u_i \cdot \nabla T = -\rho C_p U_l \frac{\partial T}{\partial x_l} + \nabla(k \cdot \nabla T) + Q \qquad (2.8)$$

Equation 2.8 is the heat transfer model for FSW process when $\rho C_p u_i \cdot \nabla T$ is total heat change, $-\rho C_p U_l \frac{\partial T}{\partial x_l}$ is the heat loss due to the tool, U_l is tool moving speed, $\nabla(k \cdot \nabla T)$ conduction heat term and Q is heat generated by heat source. Heat loss term due to the tool in Equation 2.8 is important and cannot be negligible because the FSW the PCBN tool has around 4 times higher in thermal conductivity so the majority heat will conduct through this sink rather than dissipate

in the workpiece vicinity. Heat sources in FSW are from two ways, namely, friction between tool/workpiece (Q_t) and heat from adiabatic deformation of materials (Q_b). Heat generation by friction force can be estimated by using simple frictional energy conservation and geometrical analysis of tool shoulder and pin. Heat generated by friction force can be estimated by using Equation 2.9 [14],

$$Q_{sliding} = \frac{2}{3}\pi\mu p\omega\left(\left(R_{shoulder}^3 - R_{pin}^3\right)(1 - tan\,\alpha) + R_{pin}^3 + 3R_{pin}^2 H_{pin}\right) \quad (2.9)$$

where; μ friction coefficient, p is plunging force, ω is rotational speed, α is tool shoulder cone angle (deg). This equation evaluates the pure friction heat form tool shoulder, vertical area of the pin and tip of the pin. The analytical model from Schmidt *et al*. point out that the heat is mainly generated form the shoulder (86%) the rest is from pin side and pin tip (11% and 3% respectively) [14]. This proportion is from the assumption of tool dimensions; $R_{shoulder}$ of 9 mm, R_{pin} of 3 mm, H_{pin} of 4 mm and α of 10°. The heat generated from pin tip is very small compare to other two contributions, so it can be negligible. Heat from the adiabatic transformation can be estimated by using average strain rate estimated from Equation 2.2 and Taylor-Quinney parameter (β) as [22, 23];

$$Q_b = \beta\sigma : \dot{\varepsilon} \quad (2.10)$$

When β is Taylor-Quinney parameter and σ and $\bar{\varepsilon}$ is stress tensor and strain rate tensor. The contribution from mechanical dissipation is low in FSW process of steel [13]. Nonetheless, without this term the heat generation rate is not realistic. The solution of the Equations (2.8) - (2.10) shows that the heat is generated more near tool/workpiece interface and decrease when the observed point move out of the tool affected area. Temperature of the process greatly increases in front of the tool and gradually decreases behind the tool. However, there are a lot of literature that introduced sophisticate computational model for better explain the complexity in heat transfer model of the FSW process. Those studies are beyond this work attention but the readers are encouraged to go through and get some understanding about the process.

2.4 FSW of high chromium and dispersion strengthened ferritic stainless steel

Friction stir welding of steels has been extensively studied. However, there are not many studies on high chromium steels, which appear to have complex issues when using conventional fusion welding technique for joining [24]. Han *et al*. [25] studied successfully on FSW 18Cr-2Mo ferritic stainless steel which produced by conventional casting and followed by hot rolling. The FSW tool used was cubic boron nitride embedded in tungsten-rhenium matrix. Tool parameters used were: tool rotational speed of 2000 rpm and transverse speed of 100, 130, and 160 mm/min. The tool traverse speed in which a sound weld was created was found to be 100 mm/min as shown in Figure 2.9 (a) to (c). Higher traverse speed used resulted in the root cavities defect. The SZ shows the onion ring pattern. Fine equiaxed grain structure was obtained (SZ and BM grain size was 11.9 μm and 88.5 μm). Vickers microhardness testing, shown in Figure 2.9 (d), across the weld showed that the SZ, HAZ, and TMAZ has higher hardness than the BM. Charpy impact testing showed that FSW specimen decreased 20% in toughness compare to BM.

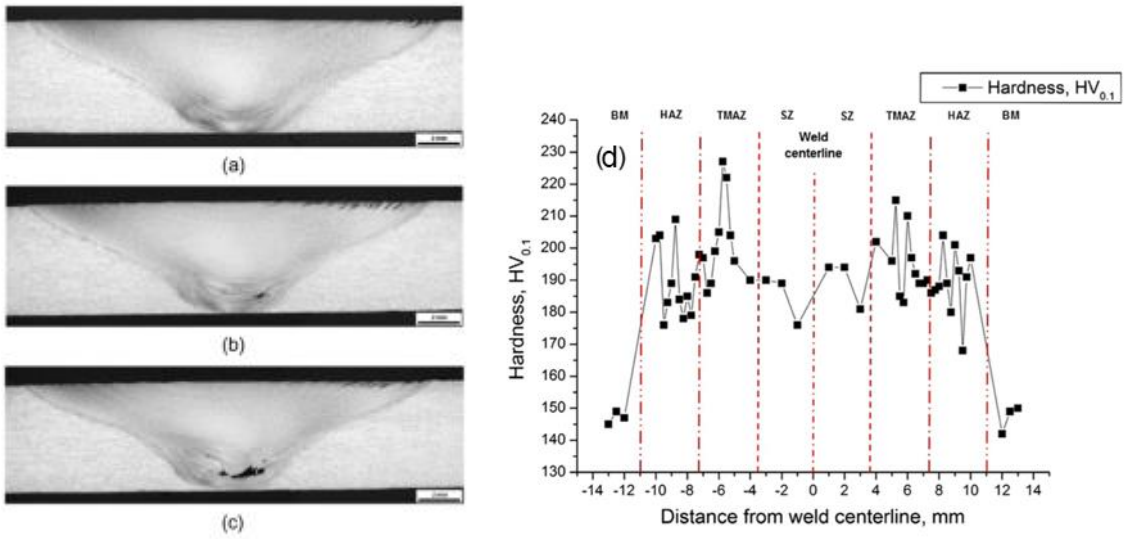

Figure 2.9. Optical macrographs of transverse sections of FSW 18Cr-2Mo steel using the traverse speed of: (a) 100 mm/min; (b) 130 mm/min; (c) 160 mm/min. (d) The corresponding Vickers microhardness profile across the weld [25].

Park *et al.* [26] studied FSW of 430 stainless steel (18 %Cr) using tool rotational speed of 550 rpm, traverse speed of 80 mm/min, tool tilt angle of 3.5^{o} and using argon shielding gas. FSW turned out to be successful. Microstructural changes in this studied was ferritic phase turned into dual phase of ferritic and martensitic phase in the SZ and TMAZ but mechanical

properties of the alloy were not degraded by FSW. Bilgin *et al.* [27] studied FSW on AISI 430 stainless steel by using parameters such as tool rotational speed of 560-1,400 RPM, traverse speed of 80-200 mm/min, compressive force of 2.0-7.5 kN, and tool tilt angles 0-3^{o}. The tool used is the simple three-flat type with non-profiled shoulder. They obtained the best result by using welding parameters as of tool rotational speed of 1,120 rpm, traverse speed of 125 mm/min, compressive force of 4.5 kN, and tilting angle of 0^{o}. In the study, microstructural examination of the SZ reveal that the SZ comprised of fine-equiaxed grain structures in contrast to the TIG welding, which created large grain structure in the weld nugget.

The latest generation of high temperature ferritic stainless steels usually contain oxide dispersion particles homogeneously distributed in the alloy matrix for improving their properties, such as creep strength, tensile strength, and/or radiation damage tolerance. These alloys are named oxide dispersion strengthened steel (ODS-steel). The commercial ferritic stainless steels of this category are PM2000, MA956, and MA957 all of which are made by mechanical alloying method. These steels are categorized as non-weldable because the lost in mechanical properties and mechanical alloyed sub-micron structure. Noh *et al.* [28] studied feasibility of FSWed (bead-on-plate configuration) high-chromium ODS Ferritic stainless steel (Fe–15%Cr–4%Al–0.5%Y_2O_3) with a PCBN tool. Using tool parameters of tool rotational speed of 800 rpm and traverse speed of 50 mm/min resulted in a sound weld. Their study also revealed that the mechanical properties is less anisotropic but shows certain degradation in mechanical properties as shown in Figure 2.10. Microstructural examination reveal that the oxide dispersion particles were largely unaffected.

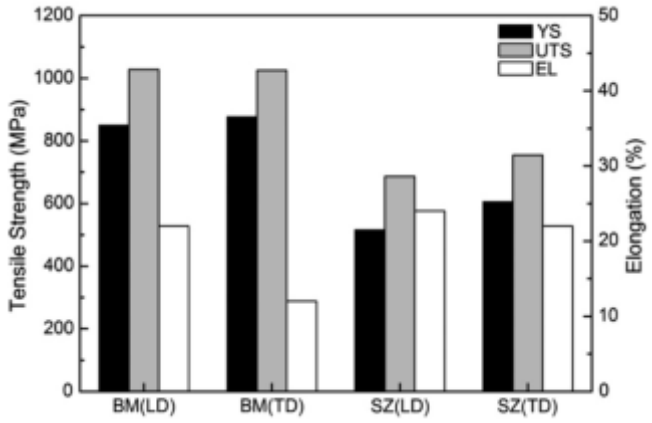

Figure 2.10. Mechanical properties of the ODS alloy from before and after FSW [28].

The PM2000 stainless steel, having composition (in wt.%) of Fe-19%Cr-5.5%Al-0.5%Ti- 0.5%Y_2O_3, processed via hot extrusion method at 1150^{o}C, was successfully welded by using FSW with PCBN tools and the used welding parameters are rotational speed of 600 rpm, and traverse speed of 50 mm/min [29]. The SZ of FSWed PM2000 shows the coarsening of oxide particles. The hardness shows softening effect by 25% in SZ. Microstructure at the root of SZ depicted the agglomeration of Al and O particles which was not occur in the middle of SZ.

Chen *et al*. [30] studied the recrystallization behavior of heat treatment (1380 ^{o}C for 1 h) effects on FSW PM2000. In their work, the BM contained elongated fine grain structures with high dislocation density. This could be the result from the process of making the alloy in that it was produced by extrusion process. Before heat treatment, SZ contained fine grains with low dislocation density because of the newly dynamic recrystallized microstructure created during FSW. The particles showed no agglomeration along the grain boundaries. Figure 2.11 (a) is the microstructure of the heat-treated FSWed PM2000 alloy which obtained by using the electron channeling effect in SEM. After heat treatment, the revealed microstructure comprised of coarser grain structure in the SZ after heat treatment. In contrast, BM grain structure is elongated grain with size in submicron range remain unchanged as shown in Figure 2.11(b). The changes in SZ that is BM are suggested to be the effects of the Zener pinning on the grain boundary in the BM and secondary recrystallization take place in SZ.

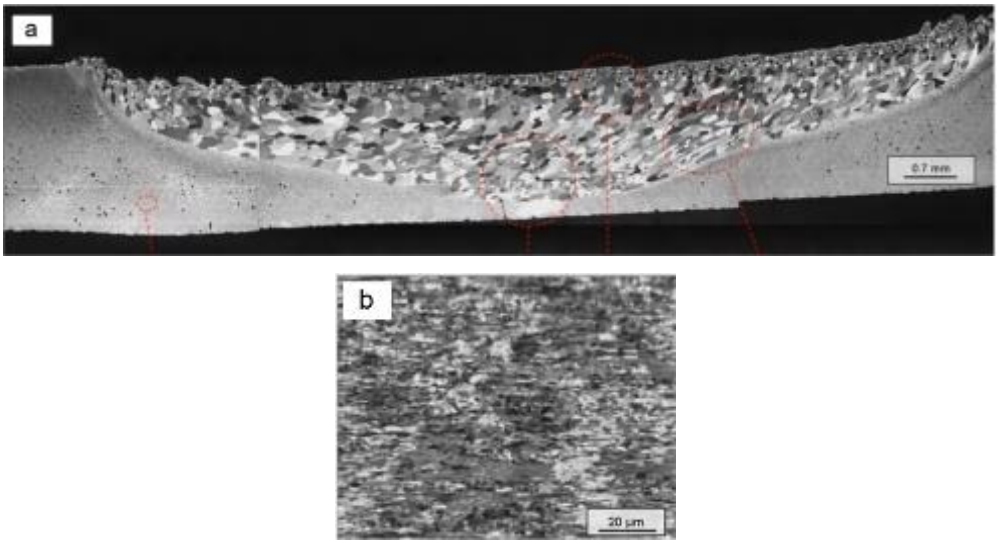

Figure 2.11. Channeling contrast image showing: (a) the weld microstructure of PM2000 after the recrystallization treatment and (b) a fine elongated grain structure showing in the non-FSW region and [30].

FSW in MA 956 was studied by Baker *et al*. [31]. They proposed the heat input index; *HI*, when

$$HI = \frac{\omega}{v} \qquad (2.11)$$

where ω is the rotational speed in RPM and v is the tool advance speed in mm/min. For successful FSW, depicted in Figure 2.12, *HI* must have minimum value of 4. MA956 alloy in this study was produced by extrusion process at 1100 ^{o}C in which alloy has a grain size of 0.89 μm. After FSW, the grain size coarsened. However, *HI* proposed in Equation 2.11 cannot be used to predict the final grain size after FSW since the real heat input is a complex dependence of different process parameters. The hardness profile across the weld is shown in Figure 2.13. The reason for softening effect in this study might be from the initial microstructure. In this study, BM has very small grain size (0.89 μm). After FSW the grain structure became coarsened to 4 – 12.5 μm. In SZ, grain size gradually decreases toward advancing side TMAZ and Retreating side TMAZ. The decreasing gradient is higher toward the advancing side than the retreating side. Texture in SZ consists of high angle grain boundaries (HAGs) and around 20% of low angle grain boundaries (LAGs). HAGs fraction increased proportional to the heat input. Dispersions were coarser in the SZ. They proposed that Y can react with Al and form yttrium aluminum garnet (YAG) and yttrium aluminum perovskite (YAP) [32].

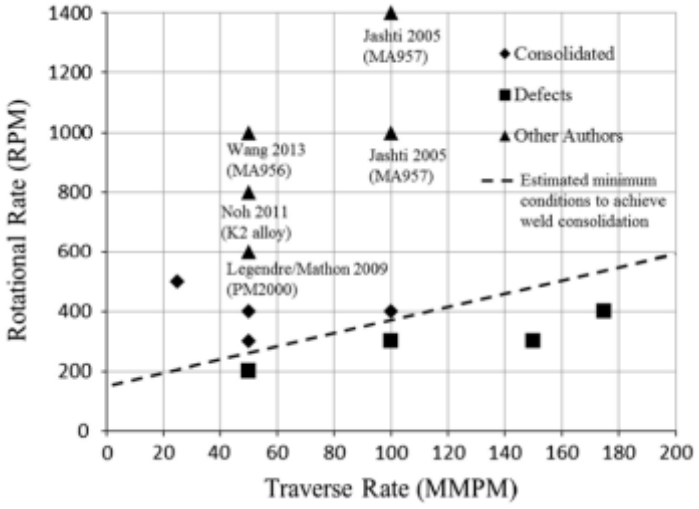

Figure 2.12. Successful rotational speed and traverse rate for FSW [31].

Table 2.1. Grain sizes and hardness of FSW MA956 [31].

FSW Condition (RPM/MMPM)	SZ Grain Size Diameter (μm)	SZ Hardness (H_V)
BM	0.89	346 ± 6.6
300/50	4.16	225 ± 4.3
400/100	6.94	221 ± 4.2
500/25	12.5	218 ± 4.2

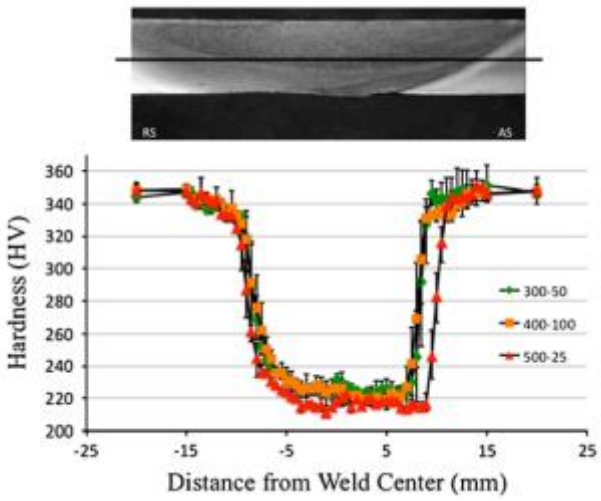

Figure 2.13. Hardness profile from different FSW conditions [31].

Miao *et al*. studied FSW MA957 (Fe, 14 %Cr, 0.9% Ti, 0.3% Mo, and 0.25% Y_2O_3) [33]. They compare FSW and electro spark deposited welding (ESD). Characterization techniques used in this work were transmission electron microscopy (TEM) and small angle neutron scattering (SANS). For both welding techniques, dispersoids were coarsened by the effects of welding. ESD welding had more effect on the dispersions than FSW. However, they suggested that those two techniques have some bias to the size of the dispersoids that can be detected, i.e., TEM can detect larger particle and is blind to smaller particle and vice versa. The change in dispersion particles is shown in Table 2.2. This deterioration in dispersoids affects the mechanical properties of the alloys by reducing the hardness as shown in Figure 2.14. Thus, FSW is found more favorable joining technique over the ESD for MA957.

Table 2.2. The average nanoscale features (NF) sizes and distribution measured by two characterization technique from the BM, FSWed and ESDed specimens [33].

NF parameters		Base metal	FSW	ESD
Average diameter (nm)	TEM	3.0	3.6	
	SANS	2.4	2.5	4.7
Number density ($\times 10^{23}/m^3$)	TEM	0.66	0.43	
	SANS	8.5	3.5	0.25
Volume fraction (%)	TEM	0.13	0.14	
	SANS	0.6	0.25	0.12

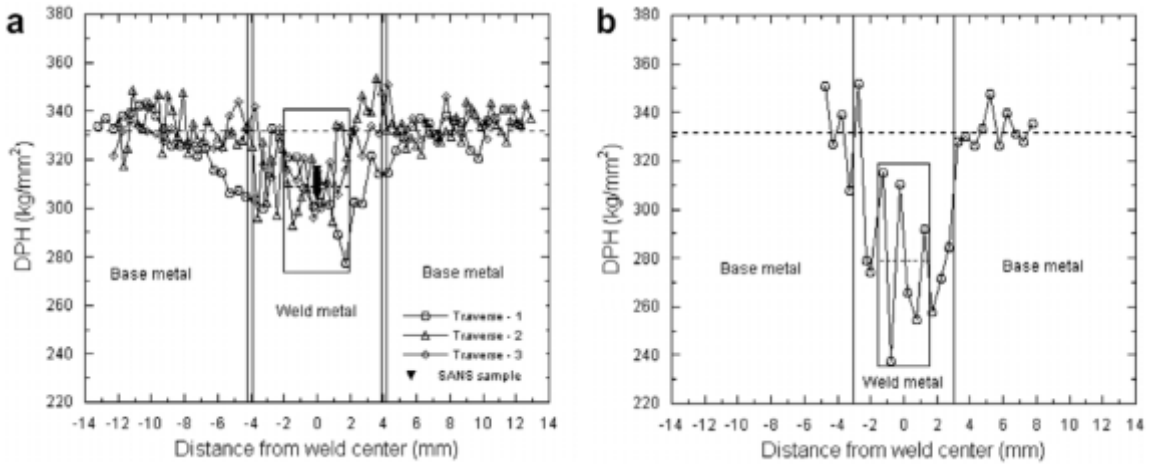

Figure 2.14. Hardness profile across MA957 weld; (a) FSW (b) ESD [33].

Study of FSW on nanostructured ferritic stainless steel, with potential for use in nuclear applications, was conducted with 14YWT nanostructured ferritic stainless steel. 14YWT has composition of Fe-14%Cr-3%W-0.4%Ti-0.3%Y_2O_3 [34]. The material can also be considered an ODS alloy which strengthens the matrix with Ti-Y-O type disperoids. The FSW parameters used were the tool rotational speed of 300 rpm and traverse rate of 76.2 mm/min. After FSW, the dispersoids increased in size and had elongated shape in the SZ and TMAZ (illustrated in Figure 2.15). After post-weld heat treatment (PWHT) at 850 ^oC for 2 min, the elongated dispersoids changed their shape to spherical shape as shown in Figure 2.16. The particle size and distribution is shown in Table 2.3. The changes in shape, size and density of the dispersoids were suggested as an effect of dissolution and re-precipitation. The nanoclusters in FSW SZ and TMAZ exhibited increment in oxygen concentration in contrast to BM in which were more

unaffected by heat treatment. There was no observed in variation of grain size or mechanical properties in this work.

Table 2.3. Size and number density of nanodispersions of FSWed MA956 [34].

Zone	Number density ($\times 10^{22}$ m^{-3})		NC size (nm)	
	As-FSW	PWHT	As-FSW	PWHT
BM	5 ± 2	5 ± 2	1.9 ± 0.6	1.6 ± 0.8
SZ	2 ± 2	20 ± 10	2.8 ± 1.6	2.0 ± 1.1
TMAZ	6 ± 3	9 ± 3	2.9 ± 1.4	2.3 ± 1.5

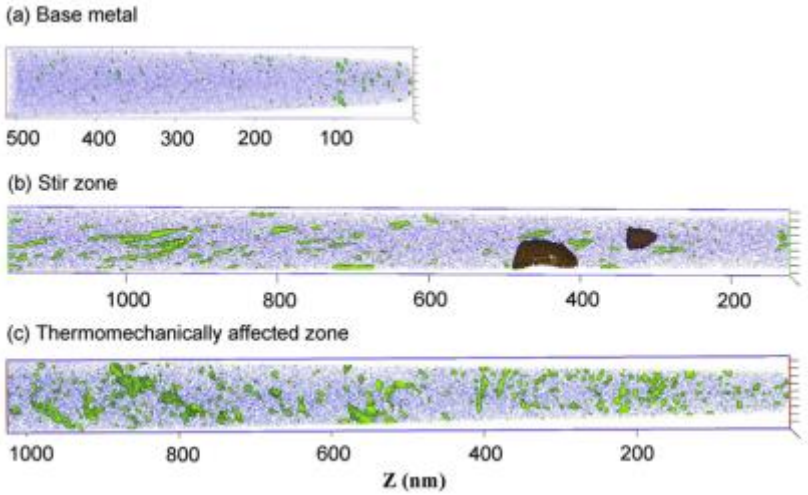

Figure 2.15. Change in size and distribution of nanoparticles after FSW [34].

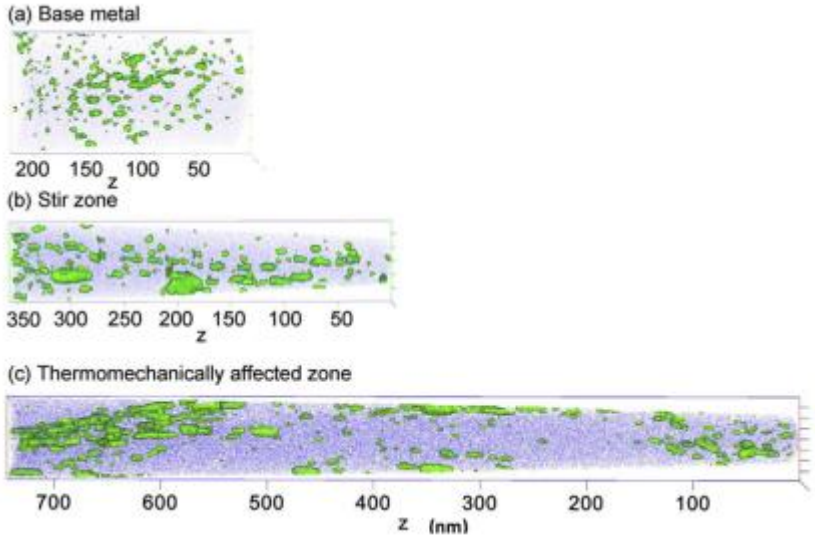

Figure 2.16. Change in size and distribution of nanoparticles after FSW and post weld heat treatment [34].

Friction stir welding explicit the applicability in joining high-chromium dispersion strengthening stainless steel. Summary of some of the works on FSW are shown in Table 2.4.

Table 2.4. Friction stir welding work on some steels

Alloy	Parameters used			Tools		Outcome	Reference
	rpm	Speed (mm/min)	Force (kN)	material	Design		
18Cr-2Mo	200	100	N/A	CBN in W-Re matrix	N/A	Root cavity formed when speed exceed 100 mm/min	25
430 SS	550	80	N/A	N/A	N/A	Martensitic transformation in SZ and TMAZ	26,27
15Cr-4Al-0.5 Y_2O_3	800	50	N/A	PCBN		Successful	28
PM2000	600	50	N/A	PCBN	N/A	Successful, nanoparticle coarsening from SZ to HAZ	29, 30
MA 956	400-500	25-100	17.8	PCBN	Convex scroll shoulder step spiral (CS4)		31, 32
MA957	130-160	150-200	N/A	N/A	N/A	Nanoparticle coarsening, Hardness drop in SZ by 7%	33
14YWT ODS	300	76.2	N/A	PCBN	16 mm threaded shoulder 6 mm diameter pin	Sound weld, change in precipitates distribution	34
316L	4-6 rad/s	0.276-0.4 mm/s	N/A	PCBN	N/A	Induce sigma phase in SZ, no change in hardness and tensile strength	29
12Cr ODS	800	60	N/A	PCBN	N/A	Hardness decrease in SZ	30

2.5 Nanostructure effects due to FSW

From previous studies, FSW is shown to have a potential to be applicable for high chromium dispersion strengthened ferritic stainless steels. The initial microstructure of the material influences the result of the weld. The ODS alloys contain stable Y_2O_3 dispersions homogeneously precipitates in the alloy matrix. The particles coarsening was found in every FSW studies [32, 34-35]. In dispersion strengthened alloys, size and distribution of the particles

are very important to the strength of the alloys because of the fine particle strengthening mechanism (e.g. Orowan strengthening mechanism and particle pinning) and particle pinning against the movement of grain boundaries depend on them. During FSW, the particles are affected by the heat from the process and undergo coarsening. The mechanism of the coarsening could also be contributed by the agglomeration of the particles [35], dissolution and precipitation [34], and phase transformation [32].

Coarsening mechanism from agglomeration of the particles is proposed by Wang *et al.* [35]. They observed the changes in dispersoids after FSW in MA754 alloys. The study suggested that the dispersoids agglomeration can be induced by the flow of material during FSW, as shown in Figure 2.17. This strain-induced agglomeration was also seen in friction welding of MA956 by Kang *et al.* [36]. The agglomeration occurs in such a way that smaller dispersoids (yttria) migrate, due to the plastic flow and combination with the larger dispersoids (alumina or Ti(C,N)).

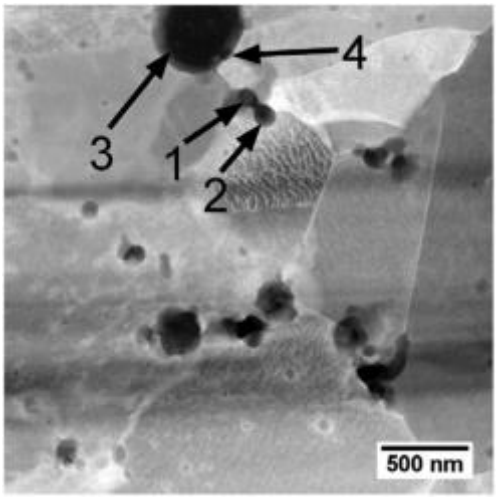

Figure 2.17. Dark field TEM shows dispersions mechanically agglomeration of FSW MA754 [35].

Dissolution and precipitation of dispersoids are usually found in FSW of Al alloys because the temperature of FSW is high enough to cause the dissolution. In ODS steels, these dispersoids are thermally stable to higher temperatures but may dissolve due to the other factors from the process. Mazumder *et al.* [34] investigated the fate of dispersoids in FSW of 14YWT ODS alloy under as-received, FSW, and PWHT conditions. After FSW, the dispersoids number density decreases and significantly increases after PWHT. Thus, the mechanism that governs the change in dispersoids is nucleation and growth.

Evolution of dispersoids could be one of the possible mechanism that governs the change in dispersoids size and distribution. In commercial ODS steels, the dispersoids are the combination of yttria and alumina. Raghavan *et al.* [37] confirmed four types of yttria-containing oxide particles generally found in commercially produced ODS alloys; i.e., cubic yttrium aluminum garnet ($5Al_2O_3•3Y_2O_3$), orthorhombic yttrium aluminum perovskite ($Al_2O_3•Y_2O_3$), monoclinic yttrium aluminum perovskite ($Al_2O_3•Y_2O_3$), and yttrium aluminum monoclinic ($Al_2O_3•Y_2O_3$). During thermally cycle in FSW process, these yttrium-domain dispersoid species can pick up the remain alumina in the BM and transformed into a new phase, Thus, the dispersoids become larger due to the change in a lattice structure.

2.6 Thermal stability at intermediate temperatures

Aluminum bearing ferritic stainless steels have been developed for the extreme environment application such as high temperature and oxidizing atmosphere. They found their application in a furnace equipment, thermocouple protecting tubes, and have a potential application as some nuclear components. Despite their superior corrosion resistant and comparable mechanical properties to Ni-base super alloys, high-Cr ferritic stainless steels experience severe embrittlement under prolonged exposure at intermediate temperatures (400 – 550 ^oC), so called 475 ^oC embrittlement. In addition, this embrittlement phenomenon can be stimulated by irradiation [38, 39]. The phenomenon need to be concerned because ferritic stainless steel is one of the candidate for using as the blanket materials for nuclear fusion reactor and considered as a new substitute fuel cladding material to conventional zirconium alloys in light water reactor (LWR)[40, 41].

In Fe-Cr binary system there is large miscibility gap between under the temperature of 550 ^oC as shown in Figure 2.18 [42]. Below this temperature there is phase decomposition phenomenon between Cr-rich α'-phase and Fe-rich α-phase. This is believed to cause embrittlement in systems that comprise of greater than 13 wt.% Cr in the temperature range of 400 – 550 ^oC. From the Fe-Cr binary phase diagram at 475 ^oC the solubility of Cr is 7 at%. Thus, the higher concentration alloys will decompose and have composition of 7 at% Cr and 96 at% Cr phases. Although, there are more uncertainty on the exact amount of Cr solubility in the phase diagram at Fe-rich side and Cr rich side [43].

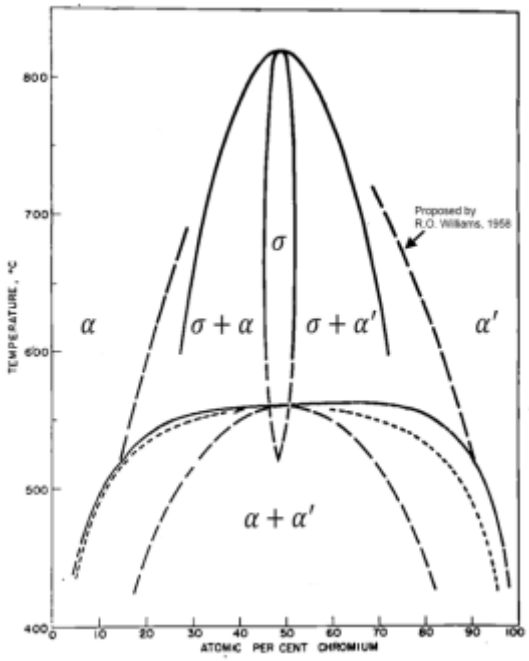

Figure 2.18. Fe-Cr Binary phase diagram at low temperature [42].

Cahn and Hilliard derived the governing equation for such phase transformation. The work resulted in a famous Cahn-Hilliard equation. From their work, it showed that the phase decomposition in solid attribute to: chemical free energy, interfacial energy and strain energy of the system [44]. When 475 ^{o}C embrittlement occur, there are the fluctuation of the composition occurred due to the energy favorable in the system, per se. The later stage of phase decomposition is agglomeration and coarsening. Microstructure changed after 475 ^{o}C embrittlement has been studied in detail in some works. Fisher *et al*. identified the phenomenon attributed to the precipitates of fine chromium rich phase called α'-phase [45]. Study by Williams confirmed this previous study. He also found that the Cr-rich cluster precipitates are anti-ferromagnetic phase and the miscibility gap is symmetrical with relatively flat top [42].

Increasing in hardness is the mechanism governs the precipitation depends on the composition and the aging condition. Spinodal decomposition favors high Cr and low temperature aging [47]. These precipitates add the dislocation motion retardants to the alloy systems so the strength increase. Hendry *et al.* reported that the embrittlement is relate to the interstitial solid solution (nitrogen) [46]. In nearly inclusion free alloys, there was no change in hardness compare to the specimen with higher amount of interstitial alloying element when they are aged at the same duration. He suggested that the embrittlement is dominated by the

degree of the lattice strain in which present of N enhances the lattice strain up to 5%. Given that Cr-N have strong chemical interaction with each other's, dislocation energy must be higher to break those bonds for further movement. The degree of embrittlement depends on several factors, namely, defect sinks [39], condition prior to the aging [48] and the mobility of the solid solution (Cr diffusion).

2.7 Limitations of FSW

Although the FSW is versatile and have the potential to become alternative joining technique to the conventional fusion welding method, the technique still has some limitations that should be addressed. Exit hole at the end of the weld is one of the obvious limitation of FSW. At the end of the FSW process, during the tool retraction phase, the volume of the material that was displaced by tool pin cannot be filled due to the nature of the process. A large forging force that is needed for FSW of the large work pieces. In order to generate enough heat for the process and be able to hold the work pieces in place, the plunging force and clamping force on the tool and workpiece must be high enough to retain the workpieces in place during the process. The flexibility compared to the conventional welding is lower. As the large force is needed for FSW process, most of the FSW needs to be done inside the workshop. Besides, since the FSW is an automatic process, the process is not preferable in welding a complicated configuration unlike the manual conventional fusion welding process. Another disadvantage of FSW is the capital cost to set up the welding workshop is high. Also, tooling cost, especially tool for FSW for high temperature alloys, is high and tool life can be affected.

2.8 Advanced characterization (transmission electron microscopy)

The limit in optical microscope is the resolution of the light source. The visible light source has the shortest wavelength of 400 nm. Thus, the smaller size features cannot be resolved. Electron microscope, on the other hand, has much shorter wavelength i.e. less than 1 nm, depends on voltage applying to the electron source. Wavelength in electron microscope can be calculated by using de Broglie relationship [49]:

$$\lambda = \frac{h}{[2m_0 eE\left\{1+\left(\frac{eE}{2m_0c^2}\right)\right\}]^{1/2}} \qquad (2.12)$$

where h is Planck's constant (6.62×10^{-34}), m_0 is the rest mass (9.1×10^{-31} kg), e is the charge on the electron (1.6×10^{-19} C), E is the accelerating voltage and c is the speed of light (3×10^8 m/s). For accelerating voltage of 200 keV the wavelength of electron is 0.0251 Å. Electron microscope was invented on this basis. The components in electron microscope is analogous to optical microscope as present in Table 2.5. The interaction of electron and specimen occurs is various way. We can divide the electron signal into 2 categories. First, the signal transmitted in the opposite side of the electron trajectory direct beam, elastically scattered electron, inelastically scattered electron and bremsstrahlung X-rays. Second, the signal occurs on the same side of the electron source. The former signal can be detected by using transmission electron microscope (TEM) and the latter by scanning electron microscope (SEM).

Table 2.5 Components in electron microscope and optical microscope.

Component	**Electron microscope**	**Optical microscope**
Light source	Electron gun	Bulb or natural light
Lens	Series of magnetic lens	Optical lens
Specimen	Electron transparent	Light transparent or reflective
Record	Digital or Film	Digital or Film

2.8.1 Electron diffraction

When we see the TEM pictures, we are seeing the whole picture from different diffraction spots. The diffraction is the interaction of wave with the small slit, in this case, it is the crystallographic plane of the crystalline specimen. The diffraction angle follows Bragg's law;

$$2dsin\theta = n\lambda \qquad (2.13)$$

when d is the (hkl) plane, λ is the incident electron wavelength and θ is diffraction angle. Nevertheless, the not all diffraction spot having the same intensity. The idea of Ewald sphere is introduced to measure intensity of the diffraction spot. Figure 2.19 and 2.20 shows the highest intensity is obtained when the diffraction spot is on the Ewald sphere, having radius of

$\lambda^{-1}$and the center is in imagined crystal. If the diffraction spot deviates from the sphere of S, the intensity will change to;

$$\frac{I_g}{I_0} = \left(\frac{F_g}{V_c}\right)^2 \frac{sin^2 \pi t s_z}{(\pi s_z)^2} \qquad (2.14)$$

where I_g is the intensity of diffracted spot, I_0 is intensity of transmitted spot, F_g is structure factors, s_z is the deviated distance from Ewald sphere at diffraction spot (excitation error) and V_c is volume of the unit cell. Since, diffraction spots pattern is unique for each crystal structure.

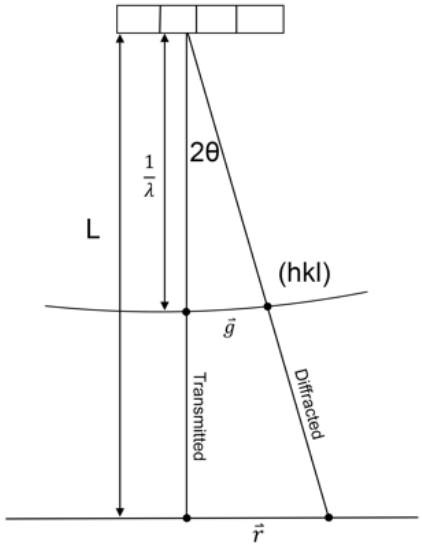

Figure 2.19. Geometry of electron diffraction

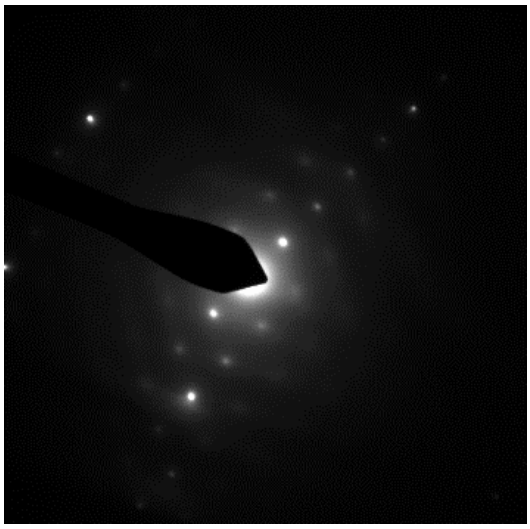

Figure 2.20. Electron diffraction pattern show the spot where the reciprocal lattice spot sit on Ewald sphere and show the intensity maxima. Note that there are no real intensity minima because of the dynamic scattering effect.

2.8.2 Imaging in TEM

In TEM, a diffraction pattern is a Fourier transform of an object, so the image is a Fourier transform of groups of diffraction pattern. There are two main methods of imaging in TEM, namely phase contrast and amplitude contrast. Amplitude contrast technique is widely used for the imaging method of thin crystalline materials. Image contrast can be estimated by kinematic approximation [49, 50] as shown below:

$$\textit{Diffracted} \qquad |\psi|_D^2 \cong \left(\frac{F}{t}\right)^2 \frac{sin^2\pi ts}{(\pi s)^2} \qquad (2.15)$$

$$\textit{Transmitted} \qquad |\psi|_T^2 \cong 1 - \left[\left(\frac{F}{t}\right)^2 \frac{sin^2\pi ts}{(\pi s)^2}\right] \qquad (2.16)$$

$$\textit{and} \qquad |\psi|_D^2 + |\psi|_T^2 = 1 \qquad (2.17)$$

where t is the specimen thickness, F is structure factor, s is excitation error. These set of equations (2.15 to 2.17) are applied to describe most of the imaging contrast in TEM and are fundamental of the TEM imaging contrast in crystalline materials.

References

1. Mishra, R. S., & Ma, Z. Y. (2005). Friction stir welding and processing. *Materials Science and Engineering: R: Reports*, *50*(1), 1-78.

2. Rai, R., De, A., Bhadeshia, H. K. D. H., & DebRoy, T. (2011). Review: friction stir welding tools. *Science and Technology of Welding and Joining*, *16*(4), 325-342.

3. Solozhenko, V. L., Kurakevych, O. O., Andrault, D., Le Godec, Y., & Mezouar, M. (2009). Ultimate metastable solubility of boron in diamond: synthesis of super hard diamond like BC 5. *Physical Review Letters*, *102*(1), 015506.

4. Zhang, Z., Liu, Y. L., & Chen, J. T. (2009). Effect of shoulder size on the temperature rise and the material deformation in friction stir welding. *The International Journal of Advanced Manufacturing Technology*, *45*(9-10), 889-895.

5. Thomas, W. M., Staines, D. G., Norris, I. M., & De Frias, R. (2003). Friction stir welding tools and developments. *Welding in the World*, *47*(11-12), 10-17.

6. Thomas, W. M., Braithwaite, A. B. M., & John, R. (2001). Skew-Stir™ technology. In *Proceedings of the 3rd International Symposium on Friction Stir Welding, Port Island, Japan*.

7. Thomas, W. M., Wiesner, C. S., Marks, D. J., & Staines, D. G. (2009). Conventional and bobbin friction stir welding of 12% chromium alloy steel using composite refractory tool materials. *Science and Technology of Welding and Joining*, *14*(3), 247-253.

8. Thomas, W. M., Johnson, K. I., & Wiesner, C. S. (2003). Friction stir welding–recent developments in tool and process technologies. *Advanced Engineering Materials*, *5*(7), 485-490.

9. Thomas, W. M., Nicolas, E. D., Smith, S.D. (2001). *Friction stir welding - tool developments*. Retrieved from http://www.twi-global.com/technical-knowledge/published-papers/friction-stir-welding-tool-developments-february-2001/

10. Lorrain, O., Favier, V., Zahrouni, H., & Lawrjaniec, D. (2010). Understanding the material flow path of friction stir welding process using unthreaded tools. *Journal of Materials Processing Technology*, *210*(4), 603-609.

11. Seidel, T. U., & Reynolds, A. P. (2001). Visualization of the material flow in AA2195 friction-stir welds using a marker insert technique. *Metallurgical and Materials Transactions A*, *32*(11), 2879-2884.

12. Smith, C. B., Noruk, J. S., Bendzsak, G. B., North, T. H., Hinrichs, J. F., Heideman, R. J., *et al.* (2000). Heat and material flow modeling of the friction stir welding process. *NIST Special Publication (SP)*, 475-488.

13. Nandan, R. G., Roy, G. G., Lienert, T. J., & Debroy, T. (2007). Three-dimensional heat and material flow during friction stir welding of mild steel. *Acta Materialia*, *55*(3), 883-895.

14. Schmidt, H. B., & Hattel, J. H. (2008). Thermal modelling of friction stir welding. *Scripta Materialia*, *58*(5), 332-337.

15. Neto, D. M., & Neto, P. (2013). Numerical modeling of friction stir welding process: a literature review. *The International Journal of Advanced Manufacturing Technology*, 1-12.

16. Uyyuru, R. K., & Kailas, S. V. (2006). Numerical analysis of friction stir welding process. *Journal of Materials Engineering and Performance*, *15*(5), 505-518.

17. Zienkiewicz, O. C., & Cormeau, I. C. (1974). Visco-plasticity—plasticity and creep in elastic solids—a unified numerical solution approach. *International Journal for Numerical Methods in Engineering*, *8*(4), 821-845.

18. Zhu, X. K., & Chao, Y. J. (2004). Numerical simulation of transient temperature and residual stresses in friction stir welding of 304L stainless steel. *Journal of Materials Processing Technology*, *146*(2), 263-272.

19. Colegrove, P. A., Shercliff, H. R., & Zettler, R. (2007). Model for predicting heat generation and temperature in friction stir welding from the material properties. *Science and Technology of Welding & Joining*, *12*(4), 284-279.

20. Nandan, R., DebRoy, T., & Bhadeshia, H. K. D. H. (2008). Recent advances in friction-stir welding–process, weldment structure and properties. *Progress in Materials Science*, *53*(6), 980-1023.

21. He, X., Gu, F., & Ball, A. (2014). A review of numerical analysis of friction stir welding. *Progress in Materials Science*, *65*, 1-66.

22. Zaera, R., Rodríguez-Martínez, J. A., & Rittel, D. (2013). On the Taylor–Quinney coefficient in dynamically phase transforming materials. Application to 304 stainless steel. *International Journal of Plasticity*, *40*, 185-201.

23. Su, H., Wu, C., & Chen, M. (2013). Analysis of material flow and heat transfer in friction stir welding of aluminium alloys. *China Weld (English Edition)*, *22*, 6-10.

24. Lippold, J., & Kotecki, D. (2005). *Welding Metallurgy and Weldability of Stainless Steels* (1st ed.). Hoboken, N.J.: John Wiley.

25. Han, J., Li, H., Zhu, Z., Barbaro, F., Jiang, L., Xu, H., & Ma, L. (2014). Microstructure and mechanical properties of friction stir welded 18Cr–2Mo ferritic stainless steel thick plate. *Materials & Design*, *63*, 238-246.

26. Park, S. H. C., Kumagai, T., Sato, Y. S., Kokawa, H., Okamoto, K., Hirano, S., *et al*. (2005). Microstructure and mechanical properties of friction stir welded 430 stainless steel. In *the Fifteenth International Offshore and Polar Engineering Conference*. International Society of Offshore and Polar Engineers.

27. Bilgin, M. B., Meran, C., & Canyurt, O. E. (2015). Optimization of strength of friction stir welded joints for AISI 430 ferritic stainless steels by genetic algorithm. *The International Journal of Advanced Manufacturing Technology*, *77*(9-12), 2221-2233.

28. Noh, S., Kasada, R., Kimura, A., Park, S. H. C., & Hirano, S. (2011). Microstructure and mechanical properties of friction stir processed ODS ferritic steels. *Journal of Nuclear Materials*, *417*(1), 245-248.

29. Legendre, F., Poissonnet, S., Bonnaillie, P., Boulanger, L., & Forest, L. (2009). Some microstructural characterizations in a friction stir welded oxide dispersion strengthened ferritic steel alloy. *Journal of Nuclear Materials*, *386*, 537-539.

30. Chen, C. L., Tatlock, G. J., & Jones, A. R. (2010). Microstructural evolution in friction stir welding of nanostructured ODS alloys. *Journal of Alloys and Compounds*, *504*, S460-S466.

31. Baker, B. W., Menon, E. S. K., McNelley, T. R., Brewer, L. N., El-Dasher, B., Farmer, J. C., *et al*. (2014). Processing-microstructure relationships in friction stir welding of MA956 oxide dispersion strengthened steel. *Metallurgical and Materials Transactions E*, *1*(4), 318-330.

32. Baker, B. W., Knipling, K. E., & Brewer, L. N. (2017). Oxide particle growth during friction stir welding of fine grain MA956 oxide dispersion-strengthened steel. *Metallurgical and Materials Transactions E*, *4*(1), 1-12.

33. Miao, P., Odette, G. R., Gould, J., Bernath, J., Miller, R., Alinger, M., *et al.* (2007). The microstructure and strength properties of MA957 nanostructured ferritic alloy joints produced by friction stir and electro-spark deposition welding. *Journal of Nuclear Materials*, *367*, 1197-1202.

34. Mazumder, B., Yu, X., Edmondson, P. D., Parish, C. M., Miller, M. K., Meyer, H. M., *et al*. (2016). Effect of friction stir welding and post-weld heat treatment on a nanostructured ferritic alloy. *Journal of Nuclear Materials*, *469*, 200-208.

35. Wang, J., Yuan, W., Mishra, R. S., & Charit, I. (2013). Microstructural evolution and mechanical properties of friction stir welded ODS alloy MA754. *Journal of Nuclear Materials*, *442*(1), 1-6.

36. Kang, C. Y., North, T. H., & Perovic, D. D. (1996). Microstructural features of friction welded MA 956 superalloy material. *Metallurgical and Materials Transactions A*, *27*(12), 4019-4029.

37. Raghavan, M., Steeds, J. W., & Petkovic-Luton, R. (1982). Convergent beam diffraction analysis of dispersoids in oxide dispersion strengthened alloys. *Metallurgical Transactions A*, *13*(6), 953-957.

38. Hardie, C. D., Williams, C. A., Xu, S., & Roberts, S. G. (2013). Effects of irradiation temperature and dose rate on the mechanical properties of self-ion implanted Fe and Fe–Cr alloys. *Journal of Nuclear Materials*, *439*(1), 33-40.

39. Soisson, F., & Jourdan, T. (2016). Radiation-accelerated precipitation in Fe–Cr alloys. *Acta Materialia*, *103*, 870-881.

40. Pint, B. A., Dryepondt, S., Unocic, K. A., & Hoelzer, D. T. (2014). Development of ODS FeCrAl for compatibility in fusion and fission energy applications. *JOM*, *66*(12), 2458-2466.

41. Guria, A. (2015). *Mechanical behavior of aluminum-bearing ferritic alloys for accident-tolerant fuel cladding applications*, Unpublished master's thesis, University of Idaho, Moscow, Idaho

42. Williams, R. O. (1958). Further studies of the iron-chromium system. *Transactions of the Metallurgical Society of AIME*, *212*.

43. Xiong, W., Hedström, P., Selleby, M., Odqvist, J., Thuvander, M., & Chen, Q. (2011). An improved thermodynamic modeling of the Fe–Cr system down to zero Kelvin coupled with key experiments. *Calphad*, *35*(3), 355-366.

44. Cahn, J. W. (1961). On spinodal decomposition. *Acta Metallurgica*, *9*(9), 795-801.

45. Fisher, R. M., Dulis, E. J., & Carroll, K. G. (1953). Identification of the precipitate accompanying 885 ^{o}F embrittlement in chromium steels. *Journal of Metals*, *5*(5), 690-695.

46. Hendry, A., Mazur, Z. F., & Jack, K. H. (1979). Influence of nitrogen on 475 C embrittlement of high-chromium ferritic steels. *Metal Science*, *13*(8), 482-486.

47. Nichol, T. J., Datta, A., & Aggen, G. (1980). Embrittlement of ferritic stainless steels. *Metallurgical Transactions A*, *11*(4), 573-585.

48. Lagneborg, R. (1967). Metallography of the 475 C embrittlement in an Iron-30 Per Cent chromium alloy. *ASM Transactions Quarterly*, *60*(1), 67-78.

49. Gareth, T., & Goringe, M. J. (1979). *Transmission Electron Microscopy of Materials*. New York: John Wiley & Sons

50. Williams, D. B., & Carter, C. B. (1996). *Transmission Electron Microscopy* (pp. 352-354). New York: Springer US.

Chapter 3: Experimental Procedures

3.1 Material

Kanthal APMT^{TM} plate is procure from Sandvik, Ins. The dimension of the as-received Kanthal APMT^{TM} plate was 34x10x0.8 cm in dimension. Kanthal APMT^{TM} is produced via powder metallurgy route by using rapid solidification to produce the alloy powder, followed by canning and hot isostatic pressing (HIP). Finally, the material is subjected to post production process such as billet machining, hot extrusion or hot rolling, depending on the products and applications. The as-received plate was procured in the hot rolled condition. The nominal composition is shown in Table 3.1.

Table 3.1. Nominal composition (in wt%) of Kanthal APMT^{TM} [1].

Fe	Cr	Al	Mo	C	N	Mn	Si	Y	Hf	Zr	Ti
Balance	23	5	3	<0.05	0.05	<0.4	<0.7	0.1	0.1	0.05	0.02

3.2 Friction stir welding

Friction stir welding (FSW) is done at the Center for Friction Stir Welding, University of North Texas, Denton, TX. This work constitutes a preliminary work on FSW of Kanthal APMT^{TM}. Thus, the FSW parameters used were determined from the experience with hot welding. In this study, FSW was done in a bead-on-plate configuration (Figure 3.1 (a)). The parameters used in this work were: tools rotational speed of 600 rpm, traverse speed of 25.4 mm/min, and forging force of 20 kN. The study area from FSWed plate was focused in the area where the temperature of the FSW is stable i.e. after 75 mm from the starting point.

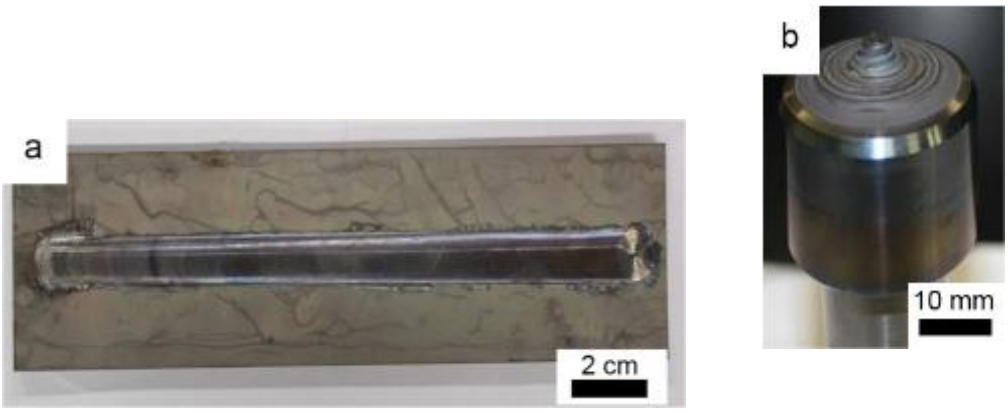

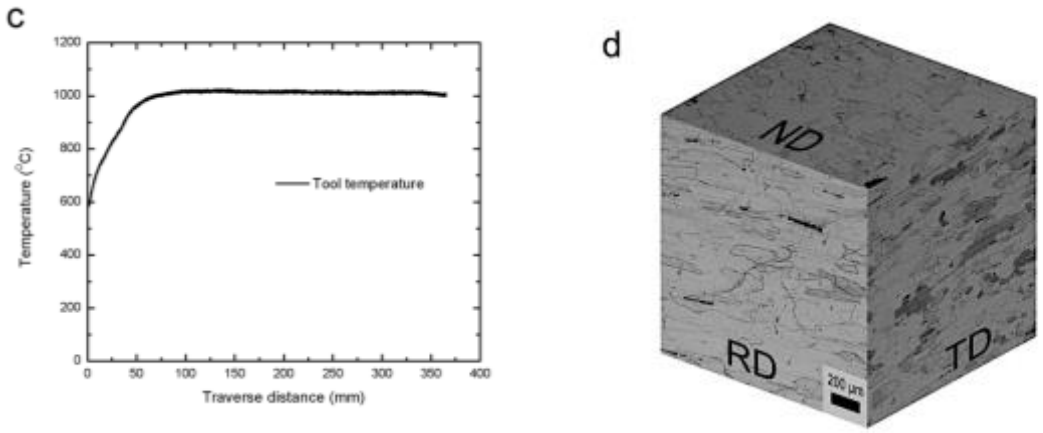

Figure 3.1. (a) successful FSWed APMT^{TM} plate, (b) PCBN FSW tool, (c) temperature profile from the process and (d) optical micrograph of as-received Kanthal APMT^{TM}.

The tool used in this work was made of PCBN. The tool configuration was convex threaded pin with scroll shoulder FSW as shown in Figure 3.1b. The Temperature profile of the work, shown in Figured 3.1c, was measured by inserting the thermocouple inside the spindle near the shoulder of the tool. The temperature reached the stable 1000^{o}C at 75 mm from the starting point until the end of the weld. Initial microstructure of as-received APMT plate is shown in Fiogure 3.1 (d)

3.3 Isothermal heat treatment (thermal aging)

The FSW and as-received APMT^{TM} specimens were aged at isothermal temperature of 475^{o}C to study the change in mechanical properties and microstructure. The specimens were sectioned from the stable temperature regions (beyond 75 mm from FSW starting point). All the specimens were isothermally aged at 475 ^{o}C for various duration, namely, 300 h, 500 h, 750 h, 1000 h, 1250 h and 1500 h in the Lindberg Blue M 8 kW tube furnace in air. After aging, the specimens were cooled at the room temperature in air. Due to the lack of materials, only base metal (BM) specimens were aged at the same temperature for 5 h, 25 h, 50 h and 150 h for observing the initial stage of the embrittlement.

3.4 Optical microscopy

The FSWed APMT^{TM} plat was cut across the welding direction to examine the microstructure features in the transverse direction. The specimen was selected from the region

where the temperature of the process was stable (1000 ^{o}C). The specimen then sectioned to have the length of 1.3 in by using a diamond wafering blade. The specimen then mounted in Bakelite using Pace Technologies Terapress hot mounting machine. The grinding and polishing steps were performed using Allied Twinprep-3^{TM} grinding disc. Grinding and polishing steps were done consecutively by using 60, 120, 240, 400, 600, 800, and 1200 grit SiC grinding paper and polished with 3 μm, 1 μm, and 0.5 μm colloidal diamond to give a mirror-finish for the metallographic specimens. The polished specimen was chemically etched for 1 minutes with Glyceregia etchant (87 Glyceregia as per ASTM E 407 designation). The composition of Glyceregia is 1-HNO_3:3-HCl:2-glycerol by volume. Optical microscopy was carried out using an Olympus PMG-3 inverse metallurgical microscope. Out of several, some micrographs were taken in raster graphics fashion at 50X magnification. Later, they were collaged together using Adobe Photoshop software.

3.5 Electron microscopy

TEM specimens were sectioned from BM and SZ. After, they were ground in the same fashion of optical micrograph specimen preparation to have the thickness down to 100 μm or below. The thinner specimen is preferred to prevent the Lorentz effect on the magnetic material. The mechanically ground specimens were then punched into standard 3 mm diameter disc specimens. Next, 3mm disc specimens were electro twin-jet polished by using Fischione model 110 electro twin-jet polisher. The solution that was used for the process consisted of 15 vol% HNO_3 + 85 vol% methanol by volume. Parameters of the successful electro twin-jet polishing process are voltage of 25 V, current of 50 mA, and electrolyte temperature around -40 ^{o}C to -50 ^{o}C. Finished specimens were examined with JEOL2010 transmission electron microscope operated at the accelerating voltage of 200 keV. The energy dispersive x-ray spectroscopy (EDS) attached to the system was used to perform chemical analysis.

Carbon replica technique was also used to isolate the dispersoid form the matrix for identification for their species. After a specimen was ground and polished, it was heavily etched by using the Glyceregia etchant. Subsequently, thin carbon layer was deposit by using vacuum evaporation carbon coating. Then, the specimen was chemically etched by using the same etchant through the carbon film for dissolve the matrix out of the dispersoid (presumably that

the dispersoids are more inert than matrix). Finally, thin carbon film was procured on the TEM grid or carbon tape for further studied by using TEM or SEM.

3.5.1 Diffraction pattern indexing

In TEM work, generally, analyzing the diffraction patterns are important. Diffraction pattern is used in many TEM studies are based on acquiring two-beam condition to various crystallographic information, obtaining bright field and dark field images, and finding specimen thickness. Two beam condition can be acquired by tilting the specimen. Then the direction of the TEM micrograph can be indexed by indexing diffraction pattern. From the geometry of electron diffraction in Figure 2.19, indexing of the plane for the diffraction spot can be done by using the relative value from the planes. When each diffraction spot is the reciprocal to the lattice plane.

$$\overrightarrow{g_i} = \frac{1}{d_i} = \frac{\sqrt{h_i^2+k_i^2+l_i^2}}{a} \qquad (3.1)$$

Thus

$$\frac{\overrightarrow{g_1}}{\overrightarrow{g_2}} = \frac{\frac{1}{d_1}}{\frac{1}{d_2}} = \frac{\sqrt{h_1^2+k_1^2+l_1^2}}{\sqrt{h_2^2+k_2^2+l_2^2}} \qquad (3.2)$$

The relative values between $\frac{1}{d_1}$ and $\frac{1}{d_2}$ are shown in Table 3.2 for BCC lattice. The ratio tables for other crystal structures system can be found elsewhere [6].

Table 3.2. Ratio table for BCC lattice [6]

	$1/d_2$	110	200	211	220	310	222	321	400	411	420	332	422
$1/d_1$													
110		1.00	1.41	1.73	2.00	2.23	2.44	2.64	2.82	3.00	3.16	3.31	3.46
200		0.70	1.00	1.22	1.41	1.58	1.73	1.87	2.00	2.12	2.23	2.34	2.44
211		0.57	0.81	1.00	1.15	1.29	1.41	1.52	1.63	1.73	1.82	1.91	2.00
220		0.50	0.70	0.86	1.00	1.11	1.22	1.32	1.41	1.50	1.58	1.65	1.73
310		0.44	0.63	0.77	0.89	1.00	1.09	1.18	1.26	1.34	1.41	1.48	1.54
222		0.40	0.57	0.70	0.81	0.91	1.00	1.08	1.15	1.22	1.29	1.35	1.41
321		0.37	0.53	0.65	0.75	0.84	0.92	1.00	1.60	1.13	1.19	1.25	1.30
400		0.35	0.50	0.61	0.70	0.79	0.86	0.93	1.00	1.06	1.11	1.17	1.22
411		0.33	0.47	0.57	0.67	0.74	0.81	0.88	0.89	1.00	1.05	1.10	1.15
420		0.31	0.44	0.54	0.63	0.70	0.77	0.83	0.89	0.94	1.00	1.04	1.09
332		0.30	0.42	0.52	0.60	0.67	0.73	0.79	0.85	0.90	0.95	1.00	1.04
422		0.28	0.40	0.50	0.57	0.64	0.70	0.76	0.81	0.86	0.91	0.95	1.00

The angles between 2 planes can be calculated by

$$cos\theta = \frac{g_1 \cdot g_2}{|g_1||g_2|} \qquad (3.3)$$

These 2 steps must be done to cross check to clarify the diffraction pattern indexing.

3.5.2 Thickness determination

For quantitative studying purpose, the specimens are determined the thickness by using convergent beam electron diffraction (CBED) method derived from the kinematic approximation [2-6]. The procedure is defocusing the two-beam condition in CBED pattern and measure intensity maxima. When two-beam condition is obtained in CBED the extinction distance can be used to obtain the specimen thickness as shown in Figure 3.2. The relationship between the extinction distance and the specimen thickness can be calculated from deviation of the fringe (s_i) by Equation 3.4. The determination of the thickness can be found from the Equation 3.5. By putting arbitrary n_k start from 1, 2, 3, ..., k. Then plot the graph between $\frac{s_i^2}{n_k^2}$ vs $\frac{1}{n_k^2}$. Regression analysis is that the Y-intercept will be $\frac{1}{t^2}$ and the slope will be $\frac{1}{\xi_g^2}$, as displayed in Figure 3.3 [6] .

$$s_i = \lambda \frac{\Delta\theta_i}{2\theta_B d^2} \qquad (3.4)$$

$$\frac{s_i^2}{n_k^2} + \frac{1}{\xi_g^2 n_k^2} = \frac{1}{t^2} \qquad (3.5)$$

where $n_k$is an arbitrary number, λ is the electron wavelength at operating voltage, θ_B is Bragg angle for the diffracting plane (hkl), θ_i is fringes spacing (from center to each intensity minima), and d is the interplanar spacing for d_{hkl}.

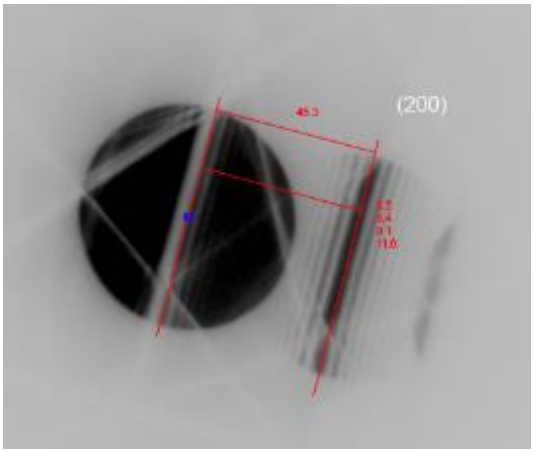

Figure 3.2. Kossel-Möllensted (K-M) fringe can be obtained by defocusing CBED in two-beams condition.

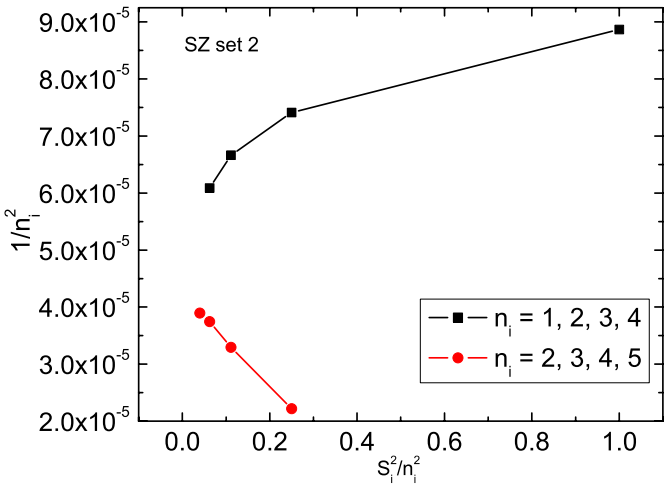

Figure 3.3. Thickness measurement plot when using arbitrary n_i start from 1 and n_i start from 2.

3.5.3 Quantitative measurement of microstructural defects

After TEM micrograph are taken, the defects in those regions i.e. dispersoids and dislocations were determined manually by assuming spherical equivalent. Particles size and distribution were counted by assuming spherical shape equivalent condition. For obtaining a statistically significant result, the quantity of size, number density, and volume fraction of the dispersion particles were determined from 6 random areas of the obtained TEM micrographs. The quantification method for determination followed the analysis method described by Higginson and Sellars [4].

3.6 Vickers microhardness testing

Vickers microhardness testing was used to assess the localized mechanical properties of the FSWed specimen. The specimen was ground and polished in the same manner as optical metallographic specimen preparation. The Vickers microhardness indentation was done by using LECO LM-100 Vickers microhardness testing machine. The indentations were done 2 mm below the surface and parallel to the top and bottom of the specimen and along 5 vertical lines from advancing side to retreating side. Each indentation was performed apart from the previous indentation no less than 4 times of the previous indentation diagonal; in this work 1 mm spacing was used.

3.7 Tensile testing

Tensile testing specimens were sectioned transversely from the welded plate and shown in Figure 3.4. The gauge length of tensile specimen was extended to 30 mm from the standard gauge length of 25.4 mm to cover all the FSW regions i.e. SZ, TMAZ, HAZ and BM. Tensile testing was done at a strain rate of 10^{-3} s^{-1} and at room temperature.

Mini-tensile specimens (gauge length of 3 mm width of 1 mm and thickness of 0.5 mm) were machined from both transverse and longitudinal directions of the welded plate. Mini-tensile testing is done in both the longitudinal direction and transverse directions. After tensile testing is done, the fracture surface of all the specimens was preserved and observed with SEM.

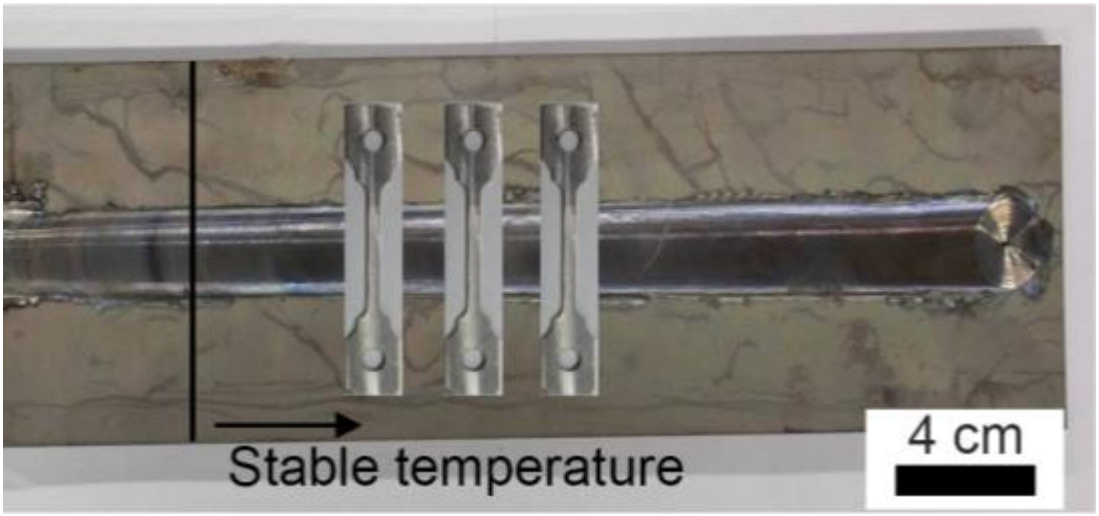

Figure 3.4. Extended gauge length (30 mm) tensile specimen sectioned parallel to the surface of the plate.

References

1. Engkvist, J., Canovic, S., Hellström, K., Järdnäs, A., Svensson, J. E., Johansson, L. G., *et al.* (2010). Alumina scale formation on a powder metallurgical FeCrAl alloy (Kanthal APMT) at 900–1,100 C in dry O_2 and in O_2+ H_2O. *Oxidation of Metals*, *73*(1-2), 233-253.

2. Delille, D., Pantel, R., Vincent, G., & Van Cappellen, E. (2002). Convergent beam electron diffraction extinction distance measurements for quantitative analysis of $Si_{1-x}Ge_x$. *Ultramicroscopy*, *93*(1), 1-9.

3. Delille, D., Pantel, R., & Van Cappellen, E. (2001). Crystal thickness and extinction distance determination using energy filtered CBED pattern intensity measurement and dynamical diffraction theory fitting. *Ultramicroscopy*, *87*(1), 5-18.

4. Higginson, R. L., & Sellars, C. M. (2003). *Worked examples in quantitative metallography*. London: Maney.

5. Williams, D. B., & Carter, C. B. (1996). The transmission electron microscope. In: *Transmission Electron Microscopy* (pp. 352-354). New York: Springer US.

6. Allen, S. M., & Hall, E. L. (1982). Foil thickness measurements from convergent-beam diffraction patterns: An experimental assessment of errors. *Philosophical Magazine A*, *46*(2), 243-253.

7. Jackson, A. (1991). *Handbook of crystallography* (1st ed., pp. 26-27). New York: Springer-Verlag.

Chapter 4: Results

4.1 Optical microscopy

Optical microscopy was first conducted to reveal overall grain structure. Figure 4.1 shows an optical montage of several micrographs providing a picture of the overall microstructural gradient present in the FSWed APMT^{TM}. It clearly shows the fine, equiaxed recrystallized grains within the stir zone (SZ), distorted grain structure in the thermal mechanical affected zone (TMAZ), and unchanged grain structure in the base metal (BM). This micrograph was done by collaging a series of micrographs taken at a magnification of 50x along the transverse cross section of the FSW specimen. The grain size was measured by the mean linear intercept technique. Average grain size in the SZ is found to be 13.7 μm while it is 72 μm in the BM. One distinct difference between the advancing side interface and the retreating side interface is the sharp change of the boundary. Interface between the advancing side of SZ and TMAZ is sharp but the retreating side interface is more diffuse. Overall observed changes in the microstructure from FSW specimen can be seen in this micrograph. To study in detail with in SZ, the optical micrographs were taken from different area of the SZ i.e. the center, root, near-surface, advancing side, and retreating side of the SZ. The grain sizes variations in each region in the SZ are depicted in Figure 4.2 and listed in Table 4.1.

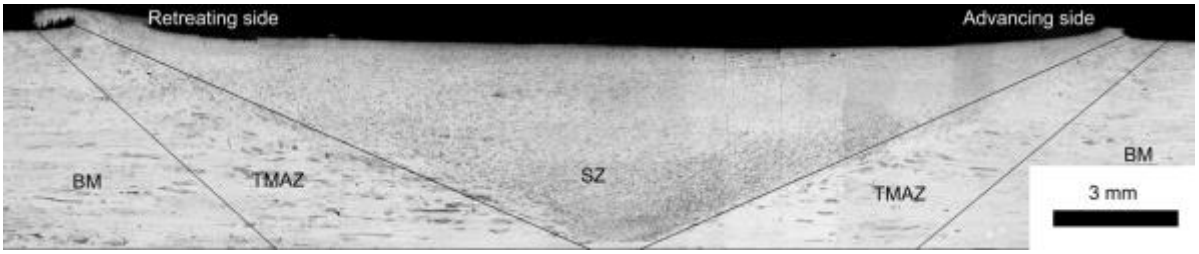

Figure 4.1. Collaged optical micrograph of FSWed Kanthal APMT^{TM}.

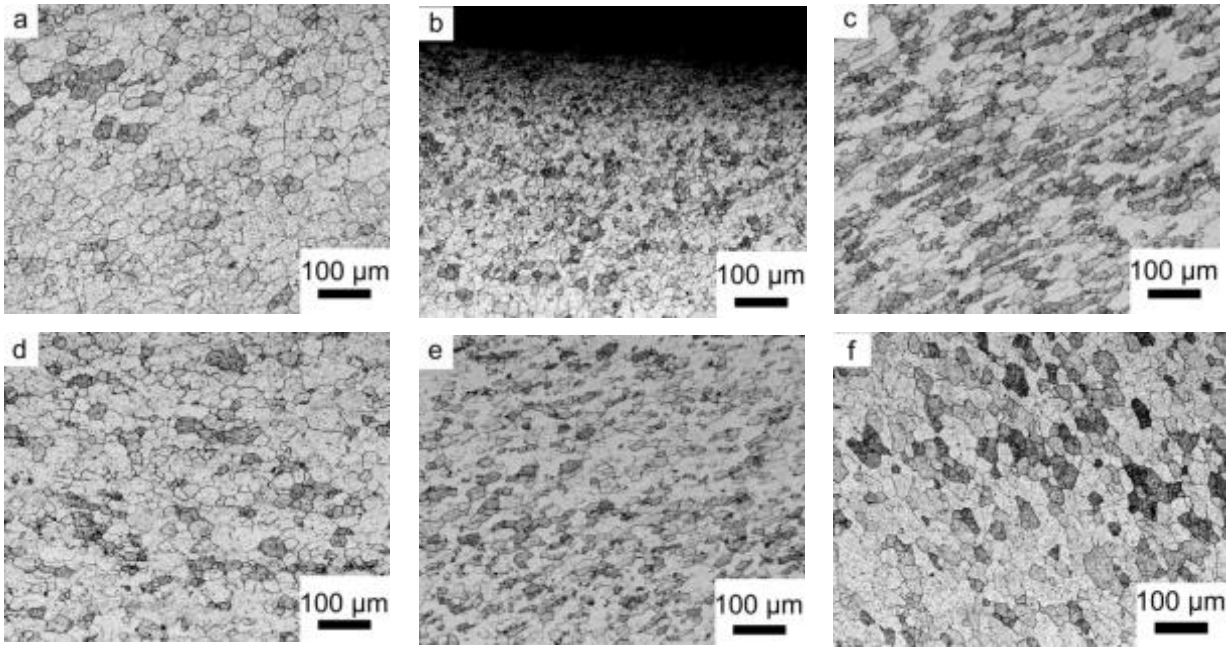

Figure 4.2. Optical macrographs of the FSWed APMT^{TM} steel: (a) Center of the weld, (b) near-surface of the weld, (c) advancing side, (d) retreating side, (e) bottom of the weld and (f) middle of the SZ in longitudinal direction.

Table 4.1. Grain sizes distribution inside the stir zone of the FSWed APMT^{TM} plate.

Area	MLI grain size (µm)
Top of the stir zone	11.8 ± 1.1
Center of the stir zone	20.4 ± 3.4
Root of the stir zone	13.0 ± 2.8
Advancing side	14.0 ± 1.7
Retreating side	13.7 ± 5.0
Center of stir zone (longitudinal)	16.1 ± 1.1

4.2 Hardness profile

Vickers microhardness is measured in the cross sections taken from the transverse direction and thickness direction of the welded APMT^{TM} plate. The hardness profile across the weld, as depicted in Figure 4.3, shows no significant change in microhardness. The vertical hardness profiles show the similar hardness trend across the thickness direction. The hardness value across the FSW is uniform and more or less similar to that of the BM. The average hardness along the FSW plate is 272 ±7 $HV_{0.5}$.

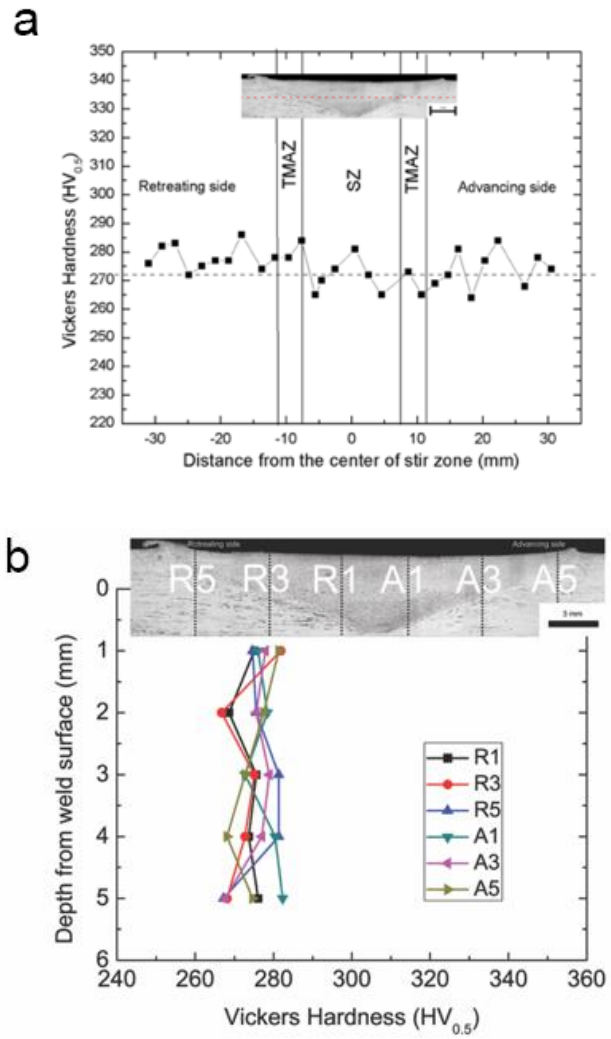

Figure 4.3. Vickers microhardness profile ($HV_{0.5}$) (a) across the weld in the transverse direction and (b) across the plate thickness.

The response in hardness for isothermal aging at 475 ºC for various durations from SZ and BM are found to be different as summarized in Table 4.2. In Figure 4.4, the increase in hardness of BM is much faster initially compared to the SZ. The peak aging time for BM is after 500 h, while hardness increase in the SZ upon aging is slow but appears to catch-up after 1000 h of aging. The peak increase in hardness from BM is 100 $HV_{0.5}$ at 750 h. At 1250 h, the peak aged of BM is reached and the hardness slightly lower. In SZ, the hardness is still increasing but in slower rate. The fitting for the hardness change is exponential decay function of $HV_t = Aexp(-t/B) + C$. When t is time in hour. In the BM, Variable parameters are -96, 166 and 373 for A, B and C respectively. In SZ, the parameters are -112, 898 and 383.

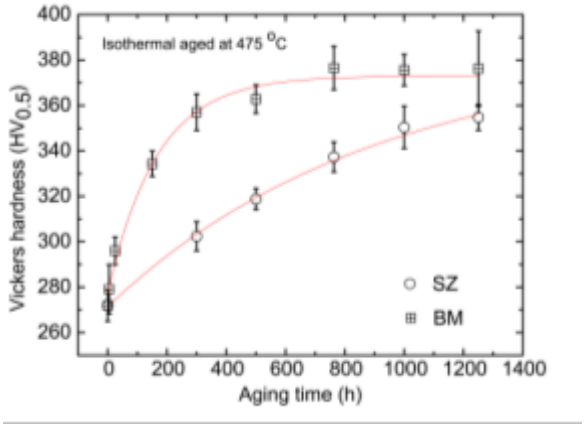

Figure 4.4. Vickers hardness profile of 300 h isothermal aging at 475 °C from SZ and BM.

Table 4.2. Vickers microhardness value from thermally aged specimen for various duration.

Time	0	5	25	150	300	500	750	1000	1250
$HV_{0.5,BM}$	272	279	296	334	357	363	376	376	371
$HV_{0.5,SZ}$	272	-	-	-	302	319	337	352	355

4.3 Tensile testing and fracture analysis

The corresponding specimen number and their tensile properties i.e. yield strength, tensile strength, %elongation and %reduction in area, are listed in Table 4.3.

Figure 4.5 (a)-(c) show the engineering stress – engineering strain curves of the parent and friction stir welded specimens. These tensile tests were performed at room temperature and strain rate of 10^{-3} s^{-1}. From the tensile stress-strain curve in Figure 4.5 (a), both as-received and FSWed specimens appear to have the same strength level. The tensile specimens (in the transverse direction of the plate) machined from the BM/T and the FSWed/T (Specimen #1 and #3) were used in the tensile test. The FSWed specimen fractured outside of the SZ essentially within the base material side. Nonetheless, the SZ specimen fractured at a higher overall strain compared to the BM.

Because of the limited material availability, more full-length tensile specimens could not be made. That is why mini-tensile specimens were machined. Another advantage of the mini-tensile specimens is that the entire specimen can be machined out from the SZ. From Figure 4.5 (b), the SZ specimen in the longitudinal direction (Specimen #5) shows higher yield strength and ductility compared to the BM/L in the same direction (Specimen #2). However,

the SZ specimen taken in the transverse direction (Specimen #4) exhibits lower strength level compared with the longitudinal SZ specimen (Specimen #5). Figure 4.5 (c) depicts the tensile behavior of both BM and SZ specimens isothermally aged at 475 ^{o}C for 300 h. Tensile testing shows that the aged APMT plate (Specimen #6) has higher yield strength (by 306 MPa) compared to the unaged specimen #1. While the ductility decreases greatly down to negligible levels, Specimen # 5 and 8 (SZ/L and aged SZ/L) show that the yield strength from the aged specimen remains more or less the same as that of the unaged specimen; albeit ductility decreases from 18% to mere 1.5%.

Table 4.3. Tensile properties of as-received and FSWed APMT^{TM}.

Specimen No.	**Specimen**	**Yield strength (MPa)**	**Tensile strength (MPa)**	**Elongation (%)**	**Reduction in Area (%)**
1	As-received/T[1] (BM/T)	594	735	6.6	7.4
2	As-received/L[2] (BM/L)	639±20	798±47	10±2.5	35.5
3	FSWed/T[1]	609	734	11.3	31.4
4	SZ-transverse[2] (SZ/T)	657±83	806±85	18±0.9	58.4
5	SZ-longitudinal[2] (SZ/L)	790±55	964±72	17.5±0.6	45.3
6	Aged APMT^{TM} plate[1] (Aged BM/T)	900	900	Nil	Nil
7	Aged FSW APMT^{TM1} (Aged FSW/T)	800	800	Nil	Nil
8	Aged SZ-longitudinal[2] (Aged SZ/L)	720	800	1.5	Nil

[1] tensile testing and [2] mini-tensile testing

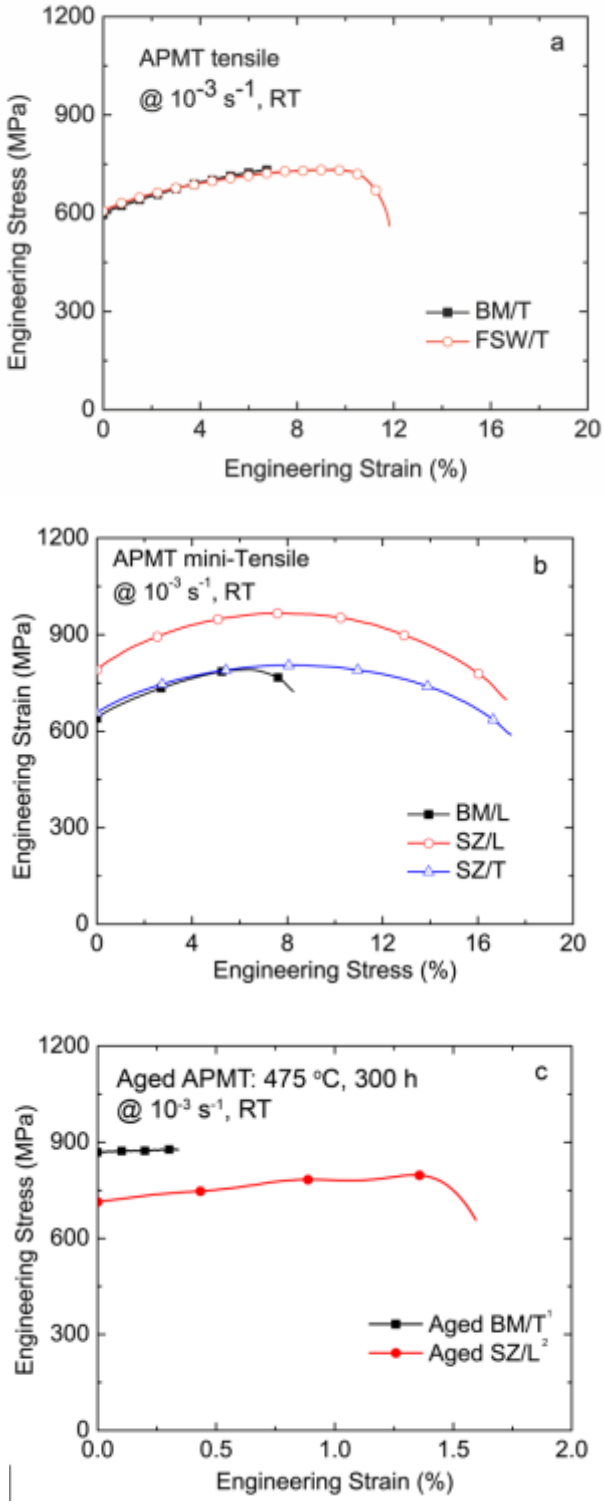

Figure 4.5. Room temperature tensile properties at strain rate of 10^{-3} s^{-1} of (b) mini-tensile testing from the BM in longitudinal direction (BM/L), the SZ in longitudinal (SZ/L) and transversal (SZ/T) direction and (c) tensile and mini-tensile testing of aged specimens. Superscript [1] describes tensile testing result and [2] denotes mini-tensile testing results.

Fractographs of the tensile testing specimens are shown in Figure 4.6. Figure 4.6 (a) shows the fracture surface of the BM/T tensile tested specimen (Specimen #1). The fracture surface shows the facet characteristics with transgranular fracture mode. No microvoids are observed from the fractograph. Figure 4.6 (b), taken from the as-FSWed specimen (Specimen #3), shows some ductile region as revealed by the presence of dimple-like features. It also exposed a lot of brittle features, which reflect the transgranular fracture mode with faceted characteristics. Figure 4.6 (c) and (d) are taken from the aged as-received and FSWed specimens (Specimen #6 and #7). Both are showing faceted fracture surface identical to each other. The pictures show brittle fracture mode.

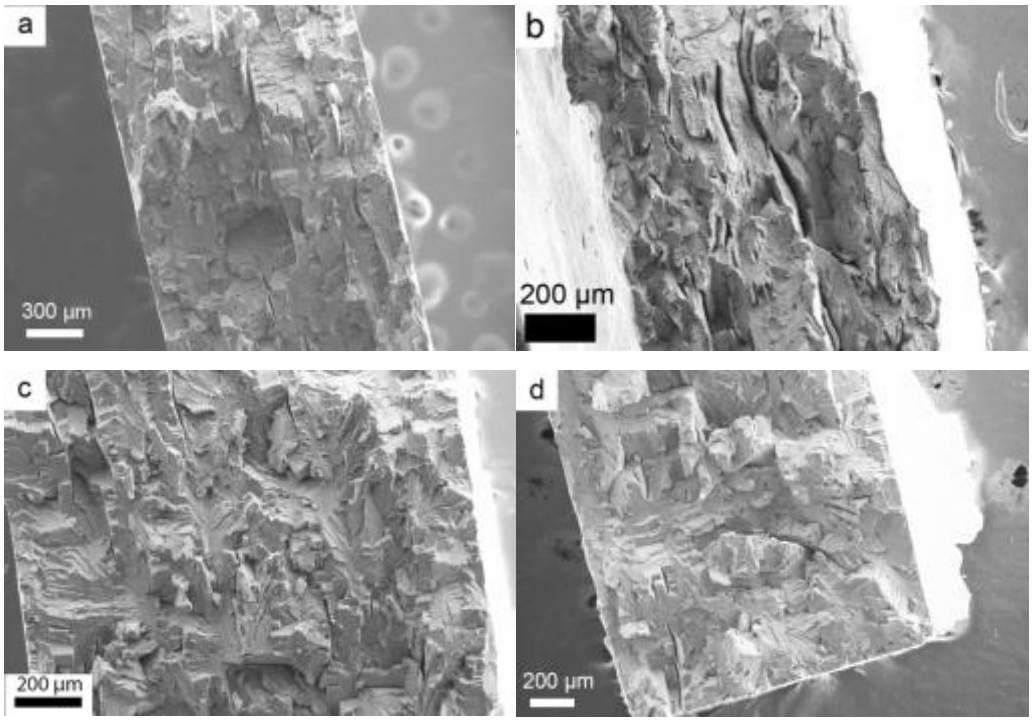

Figure 4.6. Fracture surface from tensile testing at room temperature and strain rate of 10^{-3} s^{-1} of (a) as-received and (b) FSWed APMT^{TM} (c) as-received + aged at 475 ^{o}C for 300 h and (d) FSW + aged at 475 ^{o}C for 300 h.

Figure 4.7 to 4.10 are the fractographs of the mini-tensile testing specimens. Figure 4.7 is the from the mini tensile tested of BM in longitudinal direction (Specimen #2). It shows ductile fracture contrast with the BM specimen from tensile testing in Figure 4.6 (a) which is taken from transverse direction. This can be implied that the as-received APMT^{TM} plate has anisotropy properties between transverse and longitudinal directions. Figure 4.8 and 4.9 is the

fractographs from the SZ in both longitudinal (SZ/L) and transverse directions (SZ/T). Their morphologies of the fracture are similar i.e. both show ductile fracture characteristic. This is because the grain refinement in SZ make the BM less anisotropic. Figure 4.10 is the fractograph of the SZ/L after aged for 300 h at 475 ^{o}C. The fracture shows facet fracture with equal amount of intergranular and transgranular crack.

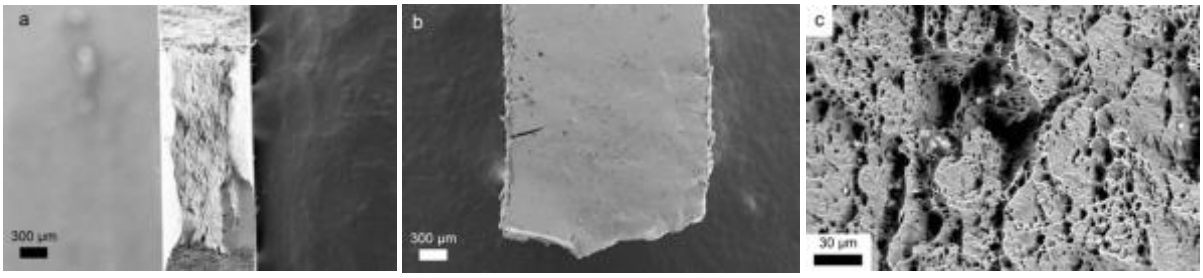

Figure 4.7. Fracture surface of BM (longitudinal direction) from mini-tensile testing.

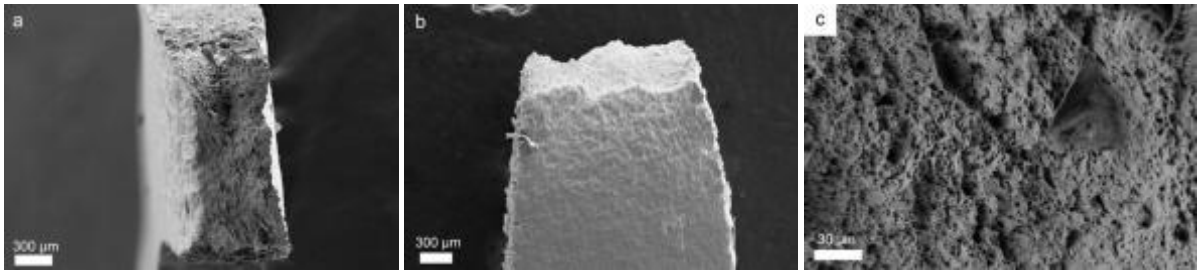

Figure 4.8. Fracture surface of SZ (longitudinal direction) from mini-tensile testing.

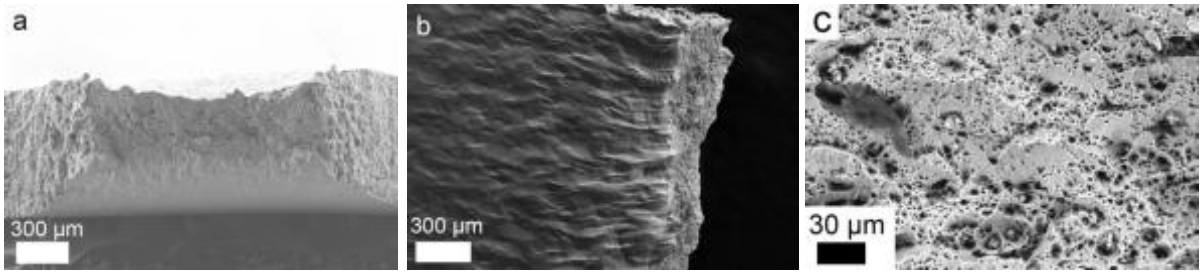

Figure 4.9. Fracture surface of SZ (transverse direction) from mini-tensile testing.

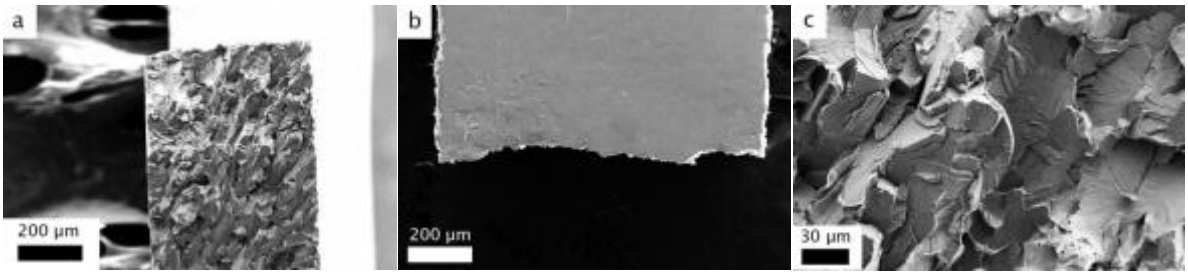

Figure 4.10. Fracture surface of 475^{o}C 300 h aged SZ (Longitudinal direction) from mini-tensile testing.

4.4 Transmission electron microscopy

TEM study shows important aspect of effect of FSW to the specimen. APMT^{TM} contain dispersoids that contributes to improve the mechanical properties. These particles determined by using energy dispersive x-rays spectroscopy (EDS), comprises of Y, Al or Hf, Zr. Figure 4.11(a) shows the BF-TEM image of the as-received APMT^{TM} plate. The microstructural features of the BM consist of high density of dislocation, and homogeneously distributed dispersoids. Figure 4.11 (b) is taken from the SZ. It shows the coarsening and agglomeration of the dispersoids and low dislocation density. Figure 4.11 (c) depicts the larger particle which is the Y-rich dispersoid. Figure 4.11 (d) shows the smaller particles that are rich composition in Hf and Zr.

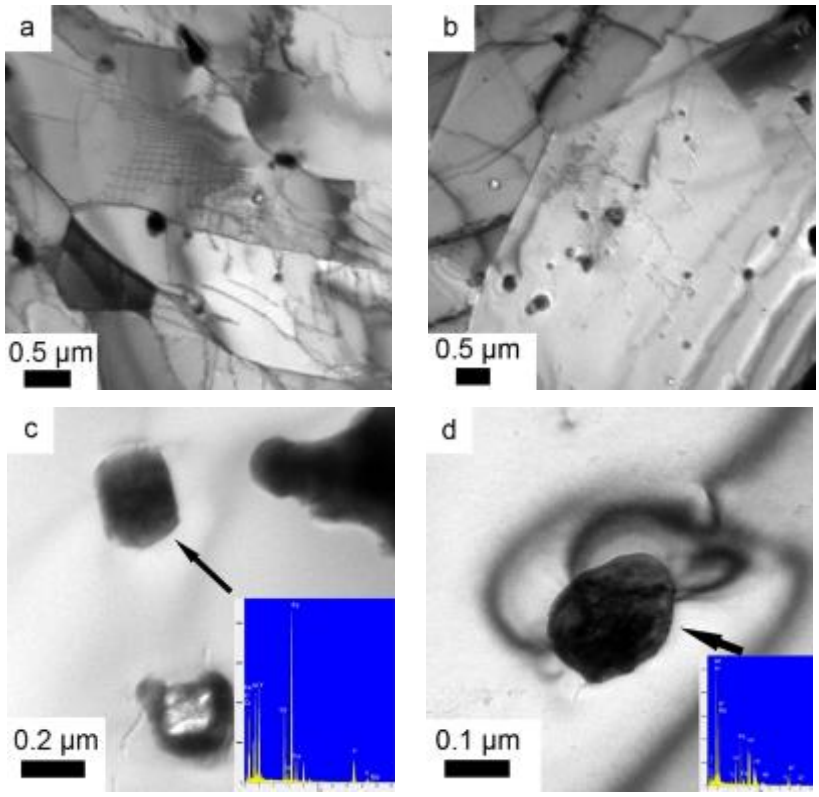

Figure 4.11. The BF-TEM micrograph of (a) BM, (b) SZ, (c) larger Y rich particle, and (d) smaller Hf, Zr rich particle.

In TEM, the EDS signal is a combination between particle signal itself and the background signal. In order to determine the precipitates species, carbon replica technique was utilized. The EDS spectrum from the carbon replica technique show that the particles consist of two types of particle i.e. yttrium aluminum garnet: YAG ($Y_5Al_{12}O_6$) and $(Hf,Zr)O_2$. EDS spectrum of matrix and some other particles are shown in Figure 4.12. The size and fraction of

dispersoid in each region of FSWed APMT^{TM} are shown in Table 4.4. Particle sizes and frequencies from specimens are shown in Figure 4.13. The distribution curve shifts to the right but maintain the normal distribution shape. In BM, the dispersoids has average size of 106 ±5 nm and volume fraction of 0.016 ±.003. In SZ, an average size of dispersoids is 147 ±26nm and volume fraction of 0.0185±.0005. From the deviation in volume fraction from both regimes, the volume fraction of BM and SZ are assumed to be constant. Smallest dispersoid in BM size is 30 nm while it is 90 nm in SZ.

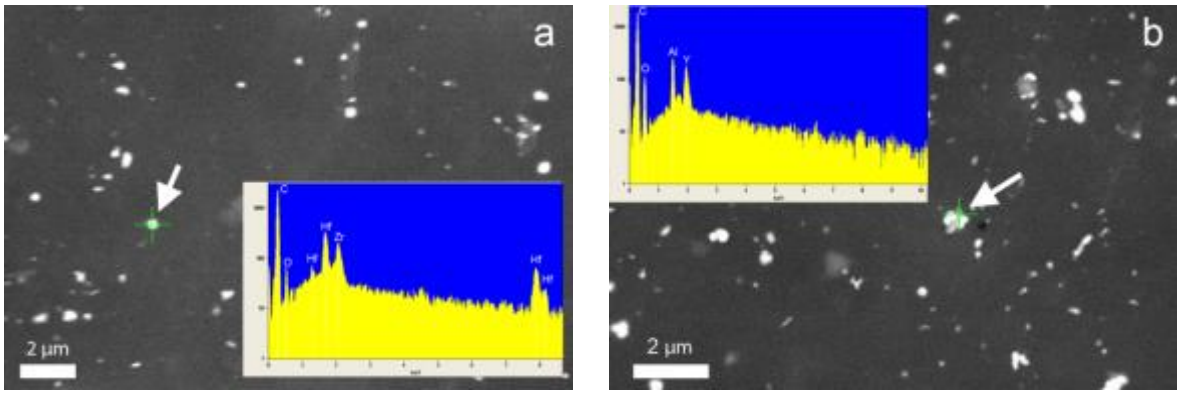

Figure 4.12. EDS spectrum (a) from the matrix, and (b) of the dispersed particles in APMT^{TM} steel.

Table 4.4. Size, distribution of dispersoids and dislocation density in each region.

Regions	Mean diameter (nm)	Volume fraction	Dislocation density (m^2)
BM	106 ±5	0.016 ±.003	4.6×10^{12}
SZ	147 ±26	0.0185±.0005	2.4×10^{12}

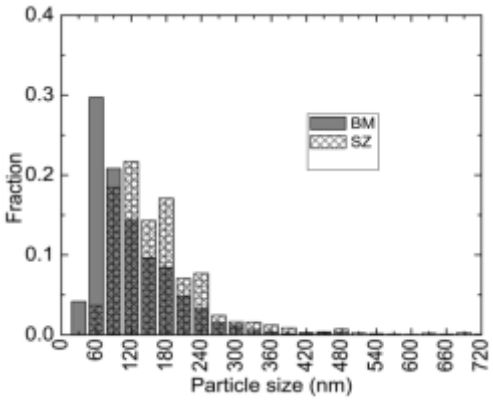

Figure 4.13. Particle size distributions of both BM and SZ.

The bright field TEM images from the isothermal aged (at 475 ^{o}C) APMT^{TM} specimens for various time periods show distinct evidence of phase separation. Figures 4.14 and 4.15 show the TEM images of the aged BM and SZ specimens, respectively. Optical microscopy could not resolve the change in microstructure in the unaged and thermally aged specimens, event after 1000 h of aging, because the size (diameter) of the precipitates is very small, such as (around 5 nm in the 1000 h aged BM specimen. TEM images of the precipitates start to become resolved when aging time exceeds 500 h. Figure 4.14(a) and 4.15(a) show that the precipitates at 500 h aging time are found to be in the irregular cluster rather than having disc shape or spherical shape. Figure 4.14(b) and (c) show the fine precipitates with sizes of 5-10 nm disperse all over the specimens. However, mottled contrast images in Figure 4.15 (b) and (c) are seen when the aging time is over 750 h for the SZ. The size of the precipitates is too small to resolve them clearly and analyze their chemical compositions.

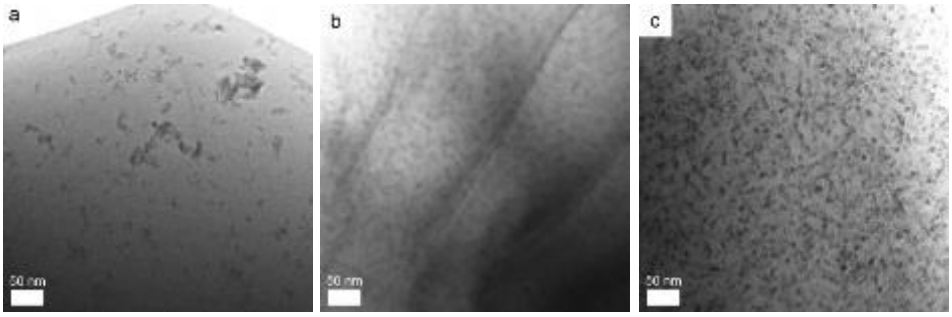

Figure 4.14. TEM micrographs showing microstructural evolution in the BM APMT^{TM} after isothermal aging for (a) 500 h, (b) 750 h, and (c) 1000 h.

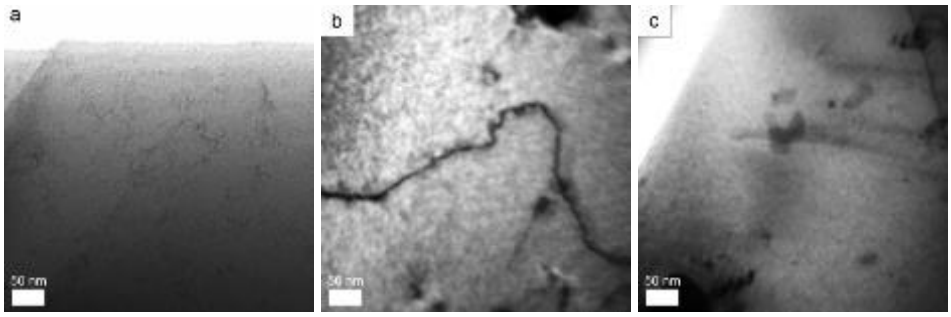

Figure 4.15. Evolution of the phase separation in the SZ after isothermal aging for (a) 500 h, (b) 750 h and (c) 1000 h.

Chapter 5: Discussion

5.1. Microstructural evolution after FSW

Friction stir welding (FSW) can be analogous to the hot extrusion process. In this work, working temperature was about 0.72 T_m where T_m is the melting point (in K) of APMT^{TM} steel (a melting point of 1500 ^oC is assumed). In addition to high strain rate, the presence of high temperature during FSW leads to dynamic recrystallization. The strain rate during the process is very high. It is reported to be in range from 3 to 180 s^{-1} [1]. Microstructures obtained from different regions in the stir zone (SZ) show variation in grain size and morphology as shown in Figure 4.2 because of the uniqueness of the material flow and thermal cycle. For example, the smaller grain structures reside on the top and bottom region of the SZ and near the interface with the thermos mechanical affected zone (TMAZ) on the advancing side. The grain refinement can be explained by using Zener-Hollomon parameter (Z) for the hot deformation of the metal as described in equation 5.1and 5.2 [2]:

$$Z = \dot{\varepsilon} exp(Q/RT) \qquad (5.1)$$

and

$$d^{-1} = a + blnZ \qquad (5.2)$$

where; $\dot{\varepsilon}$ is strain rate, Q is activation energy, R is the Boltzmann constant, and T is temperature in K, d is grain size, a and b are appropriate constants. Since the flow of material and temperature profile are rather complex, we need computational technique to approach to the issue. As discussed in section 2.2 and 2.3, the temperature of the process is the highest at the middle of the radial distance and the strain rate is highest near the interfacial of tool and materials [1]. Thus, the grain size is small at the top of area close to the surface is due to the higher strain rate. At the bottom of SZ, the temperature is low thus the grain created are smaller in size. The modelling from Palanivel *et al.* [3] shows that the strain rate at advancing side is greater than the retreating side. That reflects in slightly smaller grain structures in advancing side than that at the retreating side. That is why the mean grain size on the advancing side of the SZ is smaller than that on the retreating side. Largest grain side in the center (17.2 μm) reflects the that the strain rate in this area is low because when the material exposed to lowest strain rate compared to the advancing side and retreating side.

5.2 Hardness profile of FSW APMT^{TM}

Typical hardness profiles of FSWed steels vary depending on the process conditions, initial microstructure, and intrinsic properties of steels e.g. phase transformation during the thermal cycles, the presence of second phases, or thickness of the specimen. In FSWed 430 steel, the hardness increase by 43% in SZ. The TMAZ and HAZ hardness were as the same as the base metal (BM) one [4]. The increase in hardness was due to the martensitic formation in the SZ which had range between 40-50% while in the BM the phase contained only ferrite phase. From the work of Baker *et al.* [5], MA956 alloy showed 37% softening effect in the SZ. This effect contributed to the increase in grain size from 0.89 μm in the BM to 12.5 μm in the SZ. Also, the softening effect can be attributed to the precipitation coarsening effect. Miao *et al*. studied FSWed MA957 and found that the hardness in SZ is 7% lower than that of the BM [6]. Another work on FSW of PM2000 by Dawson *et al.* showed a softening effect by 26% in HAZ and SZ. The softening effect attributed to the larger grain structure in SZ and dispersoids coarsening [7].

In this work, despite the difference in distinctive microstructure from the optical macrographs, the hardness along the transverse direction of the weld did not vary significantly at all (just 25% variation) despite the grain structure in the SZ being much smaller than the BM but the net hardness value from these regions are similar. Thus, there must have some other contribution factors that play roles in the hardening of FSW APMT^{TM}. The rationale behind this observation will be further discussed in Section 5.4.

5.3 The fate of second phase particles after FSW

During FSW, a material receives high amount of energy from throughout heat generation and high plastic deformation. The known behaviors of material to relieve the stored energy are through recovery and recrystallization. Meanwhile, the dispersoids evolve by coarsening to decrease the surface energy to their lower energy state. Mechanisms governing the dispersoid coarsening have been proposed by following possible mechanisms i.e. nucleation and growth [8], particles agglomeration [9], phase transformation [5, 10], and Ostwald ripening [10]. In this work, quantity of EDS spectra of the dispersoids show that there are two distinct group of dispersoids in APMT^{TM} materials: smaller particles of $(Hf,Zr)O_2$, and larger particles of Y-Al-O, most likely ($Y_5Al_{12}O_6$). For APMT^{TM}, the material is designed for using at very

high temperature (1250 ^{o}C). Relative absence of smaller particles can be noted after FSW. Although, at the process temperature, it is unlikely that the dispersoids will dissolve at the temperature of 1000 ^{o}C. Recent rigorous study of evolution of dispersoids after FSW of MA956 by Baker *et al.* [6] shows that the mechanisms of coarsening are attributed to two mechanisms i.e. Ostwald ripening and phase transformation. At relatively high heat input (500 RPM and 25 mm/s), which is very similar to this process parameters (600 RPM and 25.4 mm/s) used in current study, the Y_2O_3 will pick up Al and forms complex compounds of (Y_2O_3+Al_2O_3) i.e. yttrium aluminum garnet (YAG, $Y_3Al_5O_{12}$), and yttrium aluminum monoclinic (YAM, $Y_4Al_2O_9$) and becomes explosively coarsened from 7.2 nm to 420 nm. The study shows that as the heat input is higher the fraction of YAG to YAM will be higher.

In this work, from the evidence that the particles are only YAG and (Hf,Zr)O_2 type, which both of which are thermally stable phases, the particle transformation is unlikely be the mechanism for APMT^{TM}. Ostwald ripening is likely to be a possible cause of the growth of dispersoids. Ostwald ripening involves dissolution of smaller particles, diffusion of those dissolved atoms, and growth of the larger particles. Hence, the size of the particles and interparticles spacing must change correspondingly. That is as particles become coarser, the interparticles spacing increases [11]. The volume fraction of the particle remains more or less constant, which is also true for the present work. The average particle interspacing, increasing form 671 nm to 1028 nm. Some evidence of mechanical agglomeration of particles has also been noted in the SZ as shown in Figure 4.11c. Ostwald ripening is the kinetically controlled mechanism so the morphology of the coarsened particles should not change. In contrast, the shape of some particles show smaller particle attaches to larger particle which should be from the mechanical collision during the flowing of the material during FSW. Hence, we can imply that the driven mechanism for dispersion coarsening is contributed from mechanical driven mechanism (particles agglomeration) coupled with plus kinetically driven mechanism (Ostwald ripening).

5.4 Strengthening mechanism between as-received and FSWed specimens

The theory of strengthening mechanism in polycrystalline materials is mainly related to how the dislocation mobility is affected by the inherent microstructural features of the material, which serve as obstacles to dislocation motion. Presence of any imperfections increase the stress

needed to move dislocation and accumulate plastic deformation. Strengthening mechanisms in metallic alloys is contributed by five major mechanisms: Peierls-Nabarro stress (σ_0), solid solution strengthening (σ_{SS}), dislocation strengthening (σ_D), grain boundary strengthening (σ_{GB}), and precipitation strengthening (σ_P). While there are different rules of additivity, the simplest one is the linear addition of each contributing strengthening mechanisms. Thus, the yield strength of a material (σ_y) can be described by the following relation:

$$\sigma_y = \sigma_O + \sigma_{SS} + \sigma_{GB} + \sigma_P + \sigma_D \qquad (5.3)$$

Since there is no evidence of other strengthening mechanism, such as, phase transformation and solute order changing, the strengthening mechanism is then considered from those five factors.

First contribution in strengthening mechanism is Peierls stress which arises from the atomic attraction force in the lattice. Typically, extra half plane (dislocation) resides at the lowest energy position in the lattice site as presented in Figure 5.1. Force required to move a dislocation along the slip plane is called Peierls stress, which is the function of the dislocation width and lattice constant of particular material. Hence the relationship can be written as;

$$\tau_p = \frac{2G}{1-\upsilon} exp[-2\pi a/(1-\upsilon)b] \qquad (5.4)$$

where a is lattice parameter, b is a displacement of the extra half plane (Burgers vector) and ν is the Poisson ratio [12]. The relationship of the Peierls stress intrinsic properties of material is that the lattice with widely spaced slip planes will have higher Peierls stress. However, the value from Equation 5.4 is just an estimation. The reported value found in the literature [13] is 50 MPa for ferritic steel.

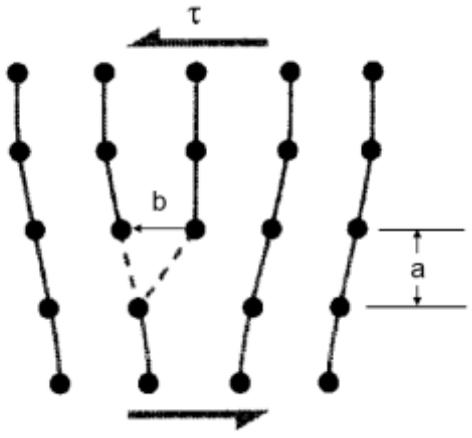

Figure 5.1. Schematic of the Peierls-Naborro stress on the movement of extra half plane through perfect lattice [14].

Solid solution strengthening is the strengthening mechanism attributed by either interstitial solid solution or substitutional solute elements. Solute elements in metal introduce strain field in lattice structure of the base metals and interacts with one of the dislocation. Contribution from each significant alloying elements is shown in Table 5.1. The following linear summation relation can be used.

$$\sigma_{SS} = \sum A_i \, C_i \qquad (5.5)$$

Where A_i is the strengthening coefficient of the i-th alloying elements, and C_i is concentration of the elements in wt%. Some strengthening coefficients of the elements are reported elsewhere [15-17]. Solid solution strengthening is affected by the solute alloying elements. So, the effect of Ti and C can be discarded because they have strong affinity to each other and form precipitate. Strength from solid solution strengthening mechanism then equals to 399 MPa.

Table 5.1. Strengthening coefficient of alloying element in steels.

Element	Strengthening coefficient (MPA/wt%)
C	5544[15]
Cr	8.5[16]
Al	Neglected [16]
Ti	-107[16]
Si	83[15]
Mo	57.3[17]
Mn	37[15]

During the dislocation movement, the grain boundary acts as the barrier on the glissile dislocation. The dislocations near the grain boundary then get retarded and dislocation itself will force the adjacent dislocations to slow down by the repulsive force of the dislocation, too, leading to dislocation pile-ups Yield strength is inversely proportional to the square root of the grain size. This is known as the Hall-Petch relation. This relationship is true until the grain size becomes very small (below 10 nm) when the strength may decrease as the grain size decreases, known as inverse Hall-Petch effect [18].

$$\sigma_{GB} = kd^{-1/2} \qquad (5.6)$$

where k is a material constant, and d is grain diameter. Value k from the literature are reported to be 15.9 MPa·mm$^{1/2}$ [16]. The contributions to the yield strength by Hall-Petch strengthening are 59 MPa in BM and 136 MPa in SZ. From Equation 5.5, it can be easily gleaned that the strength becomes higher as the grain size becomes smaller. The strengthening contribution by subgrain structure is disregarded here because of the occasional presence of this feature in the APMT^{TM} alloy plate used in this study.

Presence of fine precipitates in the alloys helps improve the strength of the alloy by impeding dislocations in their motion. To overcome these precipitates, dislocations need to either cut through or bow around them. In this study, the mean sizes of particles are rather large (106 nm in BM and 147 nm in SZ). Classical model for precipitation strengthening is Orowan strengthening (Equation 5.7) which is later modified. One of the modification that is applied for steel is Orowan-Ashby equation by consider both interparticles spacing, Taylor factor for polycrystalline material and statistical distribution of particles. Orowan-Ashby equation is written as Equation 5.8 [19]:

$$\tau_{P(Orowan)} = \frac{Gb}{L} \qquad (5.7)$$

where; G is the shear modulus (60 GPa [20]), b is Burgers vector of iron, v is Poisson ratio and L is interparticles spacing. Taylor factor is the correction factor for random orientation of the polycrystalline metals.

$$\sigma_{P(Orowan-Ashby)} = \frac{0.538Gb\sqrt{f}}{d} ln(\frac{d}{2b}) \qquad (5.8)$$

where; d is particle average diameter in μm, and f is the volume fraction of the particles present in the matrix. In this study, the sizes of particles are rather large (106 nm in BM and 147 nm in SZ). The calculated σ_P are 42 MPa in BM and 36 MPa in SZ. Although the strength distribution from dispersion strengthening is rather low in the model, it would help in the strengthening mechanism at elevated temperature where the stable dispersions pin the dislocation movement. Interaction between dislocation and precipitates is shown in Figure 5.2.

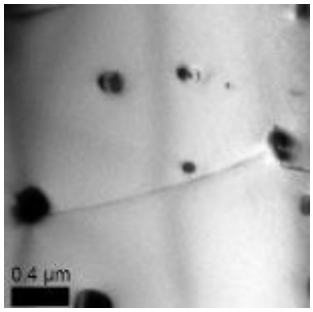

Figure 5.2. Dislocation-precipitates interaction

One of the important strengthening mechanism is work hardening or dislocation strengthening. This kind of strengthening mechanism arises due to the increase in dislocation density after deformation. This strengthening mechanism is the result of interplay among dislocations through various interactions. This result is related to the movement of the dislocations on the primary slip (maximum resolved shear stress) system and secondary slip system. These contributions are summarized below [21]:

1. passing stress of two dislocations with opposite sign on parallel plane;
2. long range stress for dislocation pile-up;
3. stress to operate Frank-Read source;
4. stress to pull out dipole from sessile jog;
5. stress to overcome repulsive force from dislocation forest;
6. stress to perform jog at dislocation forest;
7. stress necessary for a jog to create a vacancy and to separate them from glide, or by diffusion vacancy.

These contributions provide increasing in the strength of alloys. However, the distribution from each mechanism cannot be easily determined. The contribution 1 to 5 is thermally independent but depend on the configuration of the dislocations, i.e. spacing between dislocations. When dislocations are randomly aligned, the interspacing (l) is estimated to be inverse square root of the dislocation density ($\rho^{-1/2}$). The estimation of strength increase due to work hardening can be given by Equation 5.9 [22]:

$$\sigma_D = \alpha M G b \rho^{1/2} \qquad (5.9)$$

where M is the Taylor factor for polycrystalline material (for BCC, M = 2.733 [23]), ρ is dislocation density, and α is a constant reported to be 0.5 [16, 21]. Dislocation, measured from

the TEM pictures, are 4.4×10^{12} m^{-2} in BM and 2.4×10^{12} m^{-2} in SZ. Using those two values in the equation as input parameters we obtain the value of yield strength as 32 MPa in BM and 23 MPa in SZ.

Considering every strengthening contribution and using linear relation shown in Equation 5.3, we found that the yield strength in BM is 582 MPa and 644 MPa in SZ, which is within 3% error of the experimental data. Table 5.2 summarizes the model predictions while comparing them with the experimentally determined values.

Table 5.2. Contribution to yield strength of FSW APMT™.

Area	σ_O	σ_{SS}	σ_{GB}	σ_P	σ_D	$\sigma_{y(model)}$	$\sigma_{y(expriment)}$
BM (transverse)	50	399	59	42	32	582	594
SZ (transverse)	50	399	136	36	23	644	657

There is no such clear relationship between change in strength and modification in ductility. Typically, when the strength increases, the ductility decreases. After FSW, the microstructure consists of fine grain structure compared to the BM microstructure. Presence of higher fraction of grain boundaries in the SZ promotes slip near grain boundaries over the grain interior [24]. Finer grain structure also served as deformation homogenization by average the effect of stress due to dislocation pile-up at grain boundaries over the bulk of materials.

5.5 Phase transformation and embrittlement at an intermediate temperature.

Spinodal decomposition is believed to be the mechanism that governs phase decomposition under the miscibility gap as it was observed that precipitates did not nucleate at any particular microstructural defects (heterogeneous nucleation), such as dislocation, dispersoid or grain boundary. The spinodal mechanism driving force can be described by Cahn-Hilliard equation in Equation 5.10 and the kinetics of the decomposition is shown in Equation 5.11 [25]:

$$F = \int_V \left[f'(c) + \frac{\eta^2 E}{1-\nu}(c - c_0)^2 + x(\nabla c)^2 \right] dV \qquad (5.10)$$

where the first term is the contribution from chemical free energy, the second term is strain energy and the last term is interfacial energy:

$$\frac{\partial c}{\partial t} = M\left(\frac{\partial^2 f'}{\partial c^2} + \frac{2\eta^2 E}{1-\nu}\right)\nabla^2 c - 2Mx\nabla^4 c \qquad (5.11)$$

where M is the solute mobility.

FSW shows some interesting results in slowing down the microstructural evolution that leads to the thermal aging embrittlement in Kanthal APMT^{TM}. The microstructures and mechanical properties obtained from the experiments imply that FSW can slow down the precipitation rate of the α'-phase. The α' phase precipitates are clearly seen in the matrix at the aging time beyond 500 h. This change might be attributed to the difference in point defects concentration in the alloy. In some studies, the 475 ^{o}C embrittlement in irradiated ferritic steels shows that the phenomenon is accelerated by irradiation [26]. In the irradiated materials, more point defects form from the radiation damage events. These increases in point defects accelerate the diffusion rate of the α' precipitates; so the rate of the alpha-prime phase formation also increases and the effect manifests itself under irradiation at lower temperatures. In this study, the grain structure both before and after isothermal aging remains unchanged. The difference in the embrittlement rate in the BM and SZ is likely due to the effect of the point defects in the alloy. After FSW, the grain structure is refined as the result of fine equiaxed grain structure. The grain boundary is known as the point defect sinks in polycrystalline metallic alloys. Thus, it can be suggested that the point defects in the SZ is lower than that in the BM. Hence, the kinetics of α' precipitate is correspondingly slower in the SZ than the BM.

In Fe-Cr system, the mobility of Cr atoms is mainly from substitutional solute diffusion which strongly depends on the presence of vacancy. Given that the APMT^{TM} as-received APMT^{TM} plate was produced by powder metallurgy means and FSWed APMT^{TM} is in recrystallized condition, the difference in vacancy concentration can be expected that it is higher in as-received APMT^{TM}. The contrast in vacancy concentrations, thus, can make the kinetics to be slower in the SZ compared to the BM [27].

One of the possible causes for slowing down the precipitation is the presence of residual stress. FSW can induce residual stress depending on the heat input conditions and the temperature gradient involved the process. The report from a similar material such as MA956 and PM2000 shows that the residual stress in FSW plate is tension in SZ and compressive in BM [28, 29]. Lattice parameter of pure Cr is 291 pm and pure Fe is 286.65 pm. Using Vegard's law for estimate the lattice parameter in APMT^{TM}, the value is 299.66 pm. That means the Cr-

rich precipitates will cause the tensile stress to the surrounding area. Hence, the tensile residual stress deters the formation of the precipitates [30]. Effects of strain on phase decomposition was suggested by Hättestrand *et al*. The effect of coherent strain from a presence of dislocation that it can either slow down or accelerate to phase decomposition [31]. Nonetheless, this effect from residual stress might have minimal effect because the residual stresses could have been already relieved during the specimen preparation, i.e. cutting specimens in thin slices before the thermal aging treatment. So, at this point no definitive conclusion can be made regarding the effect of residual stresses.

Effects of point defect sink may also play an important role in the phase decomposition. The diffusion controlled nature of the phase decomposition makes the process strongly dependent on the concentration of point defects, which are also being annihilated by the presence of defect sinks such as dislocations, grain boundaries and so forth [26]. Higher high angle grain boundary fraction as defect sinks in the SZ should be able to play a major role in slowing down diffusion of Cr by decreasing the point defect concentrations and thus can have some effect in retarding the phase decomposition and thus α'-phase formation.

References

1. Nandan, R., Roy, G. G., & Debroy, T. (2006). Numerical simulation of three-dimensional heat transfer and plastic flow during friction stir welding. *Metallurgical and Materials Transactions A*, *37*(4), 1247-1259.

2. Ammouri, A. H., Kridli, G., Ayoub, G., & Hamade, R. F. (2015). Relating grain size to the Zener–Hollomon parameter for twin-roll-cast AZ31B alloy refined by friction stir processing. *Journal of Materials Processing Technology*, *222*, 301-306.

3. Palanivel, S., Arora, A., Doherty, K. J., & Mishra, R. S. (2016). A framework for shear driven dissolution of thermally stable particles during friction stir welding and processing. *Materials Science and Engineering: A*, *678*, 308-314.

4. Park, S. H. C., Kumagai, T., Sato, Y. S., Kokawa, H., Okamoto, K., Hirano, S., & Inagaki, M. (2005, January). Microstructure and mechanical properties of friction stir welded 430 stainless steel. In *The Fifteenth International Offshore and Polar Engineering Conference*. International Society of Offshore and Polar Engineers.

5. Baker, B. W., Knipling, K. E., & Brewer, L. N. (2017). Oxide Particle Growth During Friction Stir Welding of Fine Grain MA956 Oxide Dispersion-Strengthened Steel. *Metallurgical and Materials Transactions E*, *4*(1), 1-12.

6. Miao, P., Odette, G. R., Gould, J., Bernath, J., Miller, R., Alinger, M., *et al.* (2007). The microstructure and strength properties of MA957 nanostructured ferritic alloy joints produced by friction stir and electro-spark deposition welding. *Journal of Nuclear Materials*, *367*, 1197-1202.

7. Dawson, K., Cater, S., Tatlock, G. J., & Stanhope, C. (2014). Friction stir welding of PM2000 ODS alloy. *Materials Science and Technology*, *30*(13), 1685-1690.

8. West, M., Jahsthi, B., Hosemann, P., & Sodesetti, V. (2011). Friction stir welding of oxide dispersion strengthened alloy MA956. *Friction Stir Welding and Processing VI, TMS*, 33-40.

9. Wang, J., Yuan, W., Mishra, R. S., & Charit, I. (2013). Microstructural evolution and mechanical properties of friction stir welded ODS alloy MA754. *Journal of Nuclear Materials*, *442*(1), 1-6.

10. Bird, M. J. (2014). *Oxide evolution in ODS steel resulting from friction stir welding*. Unpublished master's thesis, Naval Postgraduate School Monterey, Monterey, California.

11. Balluffi, R. W., Allen, S., & Carter, W. C. (2005). *Kinetics of Materials*. New Jersey: John Wiley & Sons.

12. Dieter, G. E., & Bacon, D. J. (1986). *Mechanical metallurgy* (ed. 3). New York: McGraw-Hill.

13. Leslie, W. C. (1972). Iron and its dilute substitutional solid solutions. *Metallurgical transactions*, *3*(1), 5-26.

14. Roylance, D. (2001). The dislocation basis of yield and creep. *Modules in Mechanics of Materials*, 1999-2001.

15. Liu, G. (2003). Designing with carbon-, low-, and medium-alloy steels. In G.E. Totten (Ed), *Handbook of Mechanical Alloy Design* (pp. 73). New York: Marcel Dekker.

16. Wang, J., Yuan, W., Mishra, R. S., & Charit, I. (2013). Microstructure and mechanical properties of friction stir welded oxide dispersion strengthened alloy. *Journal of Nuclear Materials*, *432*(1), 274-280.

17. Guria, A. (2015). *Mechanical behavior of aluminum-bearing ferritic alloys for accident-tolerant fuel cladding applications*, Unpublished master's thesis, University of Idaho, Moscow, Idaho.

18. Meyers, M. A., Mishra, A., & Benson, D. J. (2006). Mechanical properties of nanocrystalline materials. *Progress in Materials Science*, *51*(4), 427-556.

19. Gladman, T., Dulieu, D., & McIvor, I. D. (1999). Structure/property relationships in high-strength micro-alloyed steels. *Material Science and Technology: MST: a Publication Institute of the Institute of Metals*, *15*, 30-36.

20. Wasilkowska, A., Bartsch, M., Messerschmidt, U., Herzog, R., & Czyrska-Filemonowicz, A. (2003). Creep mechanisms of ferritic oxide dispersion strengthened alloys. *Journal of Materials Processing Technology*, *133*(1), 218-224.

21. Hirsch, P. B. (1975). Work hardening. *Physics of Metals--Defects, Cambridge University Press, 1975, 2, 189-246*.

22. Pande, C. S. (2001). Strain hardening in FCC metals and alloys. *Materials Science and Engineering: A*, *309*, 328-330.

23. Rosenberg, J. M., & Piehler, H. R. (1971). Calculation of the Taylor factor and lattice rotations for bcc metals deforming by pencil glide. *Metallurgical Transactions*, *2*(1), 257-259.

24. Valiev, R. Z., Alexandrov, I. V., Zhu, Y. T., & Lowe, T. C. (2002). Paradox of strength and ductility in metals processed by severe plastic deformation. *Journal of Materials Research*, *17*(01), 5-8.

25. Cahn, J. W. (1961). On spinodal decomposition. *Acta Metallurgica*, *9*(9), 795-801.

26. Soisson, F., & Jourdan, T. (2016). Radiation-accelerated precipitation in Fe–Cr alloys. *Acta Materialia*, *103*, 870-881.

27. Capdevila, C., Miller, M. K., Pimentel, G., & Chao, J. (2012). Influence of recrystallization on phase separation kinetics of oxide dispersion strengthened Fe–Cr–Al alloy. *Scripta Materialia*, *66*(5), 254-257.

28. Mathon, M. H., Klosek, V., De Carlan, Y., & Forest, L. (2009). Study of PM2000 microstructure evolution following FSW process. *Journal of Nuclear Materials*, *386*, 475-478.

29. Brewer, L. N., Bennett, M. S., Baker, B. W., Payzant, E. A., & Sochalski-Kolbus, L. M. (2015). Characterization of residual stress as a function of friction stir welding parameters in oxide dispersion strengthened (ODS) steel MA956. *Materials Science and Engineering: A*, *647*, 313-321.

30. Schalk, N., Mitterer, C., Keckes, J., Penoy, M., & Michotte, C. (2012). Influence of residual stresses and grain size on the spinodal decomposition of metastable Ti 1− x Al x N coatings. *Surface and Coatings Technology*, *209*, 190-196.

31. Hättestrand, M., Larsson, P., Chai, G., Nilsson, J. O., & Odqvist, J. (2009). Study of decomposition of ferrite in a duplex stainless steel cold worked and aged at 450–500 C. *Materials Science and Engineering: A*, *499*(1), 489-492.

Chapter 6: Conclusion

Kanthal APMT^{TM} is a high chromium, aluminum bearing ferritic stainless steel produced by powder metallurgy process. This alloy has promising corrosion/oxidation resistance in elevated temperature in dry air and steam environment. Although it is designed for high temperature application e.g. in high temperature furnaces or thermocouple tubes, it is considered to have potential to replace the conventional zirconium alloy in nuclear fuel cladding material. Despite potential for various applications, Kanthal APMT^{TM} is not suitable for applying fusion welding technique. Hence, this study evaluated the applicability of friction stir welding (FSW), a solid-state welding technique. Friction stir welding in this study is done in a bead-on-plate configuration by using parameters; tool rotational speed of 600 rpm, tool traverse speed of 25.4 mm/min and plunging force of 20 kN. The result was a flawless weld. The welded specimen is rigorously studied by using various microstructural characterization (optical and electron microscopy) techniques and mechanical properties testing, i.e., microhardness testing and tensile testing. The following salient conclusions were made:

1. After FSW, the grain structure is changed from larger elongated grains, typical of the hot rolled plate, to a fine, equiaxed, dynamically recrystallized grain structure.

2. Vickers microhardness indentation testing shows more or less constant hardness throughout the cross section of the weld.

3. Room temperature property is improved in the stir zone regime (SZ) compared to the base metal (BM).

4. Both BM and SZ materials exhibited thermal aging embrittlement at room temperature tensile testing upon thermally aging those at 475 ^{o}C for 300 h. FSW modified the microstructure of the alloys, thereby slowing down the degree of thermal aging embrittlement (475^{o}C embrittlement).

From these preceding observations, FSW demonstrates its applicability for Kanthal APMT^{TM}. Furthermore, the technique is likely to be useful with the other FeCrAl alloys or high chromium alloys. However, the response to thermal aging embrittlement in FSW/SZ material needs to be still examined in detail.

Chapter 7: Future Work Recommendations

There are more tasks to do on this work since the friction stir welding (FSW) in this work shows its potential as a solid state joining technique for Kanthal APMT^{TM}. In the present work, only one set of parameters is observed. The parameters of FSW can be changed to study the relationship of FSW parameter and microstructural features as a function of each parameter. Thus, there is a need for developing a process window.

Because Kanthal APMT^{TM} is for high temperature applications, the behavior of FSWed specimen needs to be studies at high temperature, for the properties such as creep strength and high temperature oxidation resistance to simulate the properties of the alloy in their working load-temperature region. One of the important aspects of in metal welding is the development of residual stresses, which can impact the weld performance. However, in this work we have not studied the residual stress. So, it should be considered as future work recommendations. .

Thermal stability of FSWed specimen needs to be studied in detail so that we get a better understanding whether there is any process window that is more conducive for resisting the thermal aging embrittlement phenomenon. FSW really does retard the embrittlement effect. Atomic level microscopy techniques such as atom probe tomography (APT) and high resolution transmission electron microscopy (HRTEM) could be applied to study this fine-structure features (such as alpha prime phases) and relate the microstructural features with the kinetics of aging and embrittlement.

Appendix I: Statistical Means to Quantify the Dispersoids by Thin Foil Analysis

1. Determine the foil thickness by using the convergent beam electron diffraction as discussed in Section 3.5.2.
2. Obtain bright field transmission electron microscopy image.
3. Measure the size of the particles by using equivalent circle assumption (spherical particle shape is assumed).

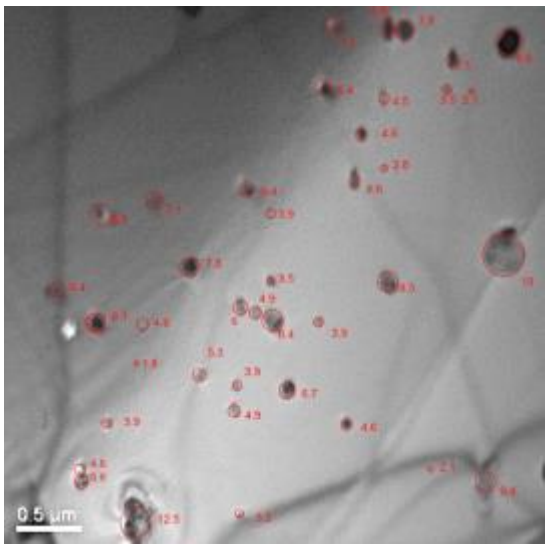

Figure 8.1. Equivalent circles represent the dispersoid particle sizes.

4. Group the particles into certain size ranges by using the largest size for upper limit of the group for example each group is divided by 30 nm in size as shown in Column 2 in Table 8.1.
5. Calculate the number of particles per unit area in Column 4 and calculate the area fraction of each group in Column 5.

$$N_{A(j)} = \frac{n(j)}{A}. \qquad (8.1)$$

6. Calculate the number of particles per unit volume and volume fraction by using thickness obtained from Step 1and using the following equation:

$$N_{V(j)} = \frac{N_{A(j)}}{(t+\left(j-\frac{1}{2}\right)\Delta)}, \qquad (8.2)$$

where Δ is the range of each data group (in this case 30 nm), t is the specimen thickness obtained from Step 1, and j is the corresponding group number; e.g. 1, 2, 3, ... n

7. Average particle size can be determined by using

$$\bar{D}_v = \sum_{j=1}^{n} \frac{\sum N_{V(j)} \times \left(j - \frac{1}{2}\right)\Delta}{\sum N_{V(j)}} \qquad (8.3)$$

8. Average volume fraction can also be calculated by the following relation:

$$V_f = \frac{\pi}{6}\Delta^3 \sum N_{V(j)} \left(j - \frac{1}{2}\right)^3 \qquad (8.4)$$

Table 8.1. Table for doing particle quantification

1	2	3	4	5	6	7
Size group (j)	Upper diameter (nm)	Count	N_A (μm^{-2})	Area Fraction; A_f (%)	N_V (μm^{-3})	Volume Fraction; V_f (%)
1	30	0	0.00000	0	0	0
2	60	11	0.05714	4	0.28145974	6
3	90	51	0.26490	21	1.13693043	26
4	120	53	0.27529	21	1.046742256	24
5	150	31	0.16102	13	0.549558221	13
6	180	37	0.19219	15	0.595002564	14
7	210	11	0.05714	4	0.161859284	4
8	240	17	0.08830	7	0.230552472	5
9	270	8	0.04155	3	0.100614268	2
10	300	4	0.02078	2	0.04690033	1
11	330	3	0.01558	1	0.032944259	1
12	360	6	0.03117	2	0.061958786	1
13	390	2	0.01039	1	0.019490475	0
14	420	1	0.00519	0	0.009225953	0
15	450	2	0.01039	1	0.01751842	0
16	480	2	0.01039	1	0.016674837	0
17	510	1	0.00519	0	0.007954382	0
18	540	0	0.00000	0	0	0
19	570	1	0.00519	0	0.007285009	0
20	600	0	0.00000	0	0	0
21	630	1	0.00519	0	0.006719549	0
22	660	0	0.00000	0	0	0
23	690	2	0.01039	1	0.012471096	0
24	720	0	0.00000	0	0	0
25	750	1	0.00519	0	0.005816586	0

26	780	0	0.00000	0	0	0
27	810	1	0.00519	0	0.005450379	0
28	840	0	0.00000	0	0	0
29	870	0	0.00000	0	0	0
30	900	1	0.00519	0	0.004980069	0
Summary		247	1.28297	100	4.358109365	100

Appendix II: Other Characterization Work

X-ray diffraction experiment was done to determine the phase changes induced by friction stir welding (FSW). The result shown in Figure 9.1 depicts that no phase change took place during FSW. Kanthal APMT^{TM} consists of mainly ferrite phase (BCC).

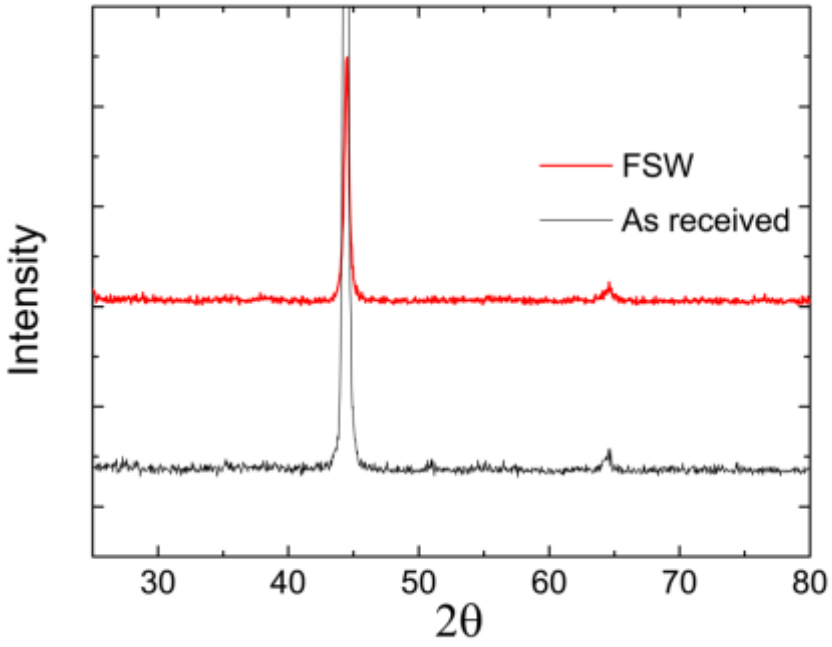

Figure 9.1. XRD analysis from as-received and friction stir welded (FSWed) specimen

Atom probe tomography experiment was performed to identify the phase separation in thermally aged APMT and FSWed APMT plate. Three-dimensional reconstruction maps from the samples isothermally aged at 475 ^{o}C for 300 h of stir zone (SZ) and base metal (BM) show that the phase decomposition in the BM is much more severe than that of the SZ as shown in Figure 9.2 (A), (B) and Figure 9.3 (A), (B). Precipitate chemical profile of aged-BM (Figure 9.4) sample shows that the Cr concentration of precipitates is 67 at.%, whereas the concentration of Cr within precipitates in the aged-SZ sample in Figure 9.5 shows that the composition of Cr is 58 at.%.

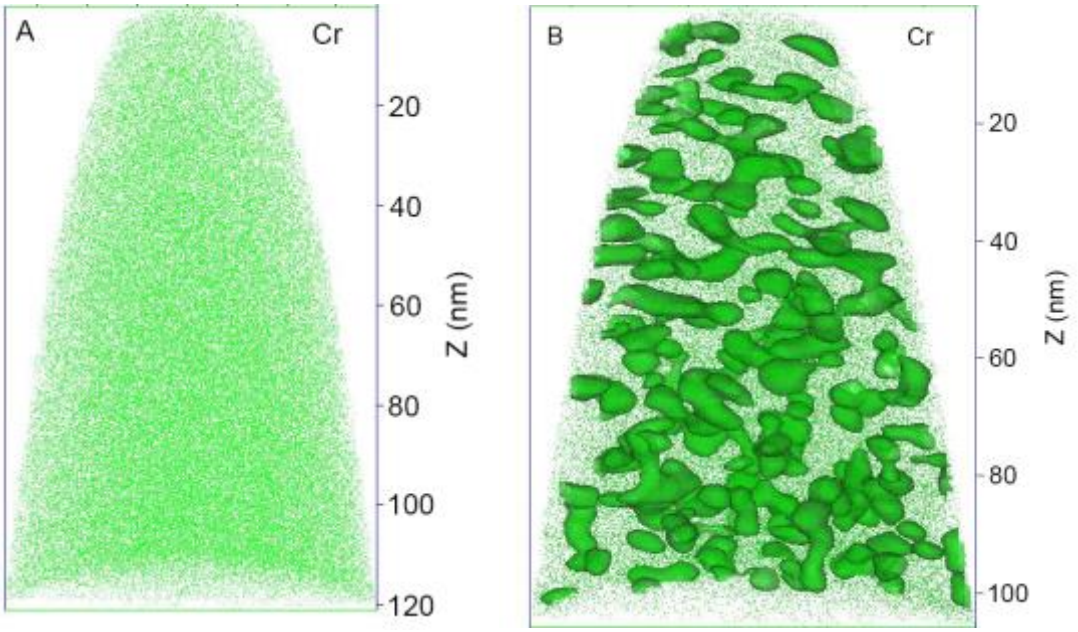

Figure 9.2. 3D reconstructed pictures from (a) unaged base metal (BM) and (b) 300 h aged BM.

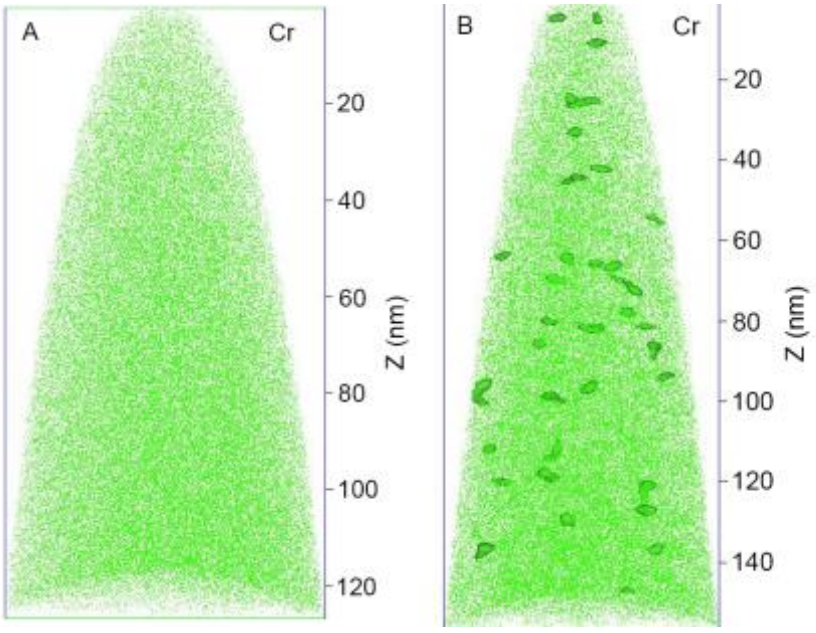

Figure 9.3. 3D reconstructed pictures from (a) unaged stir zone (SZ) and (b) 300 h aged SZ.

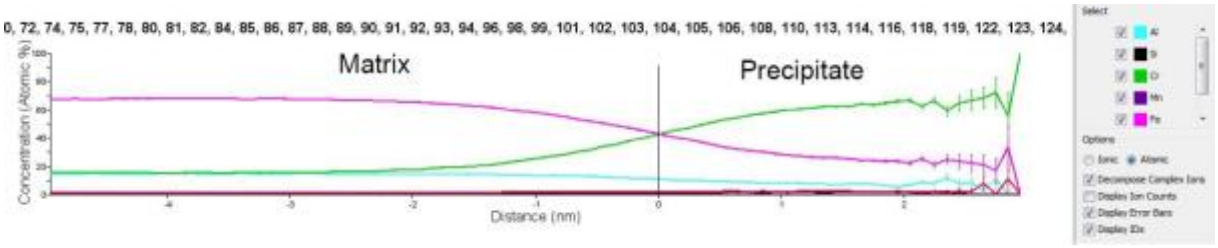

Figure 9.4. Precipitate chemical composition profile from aged BM and its interface.

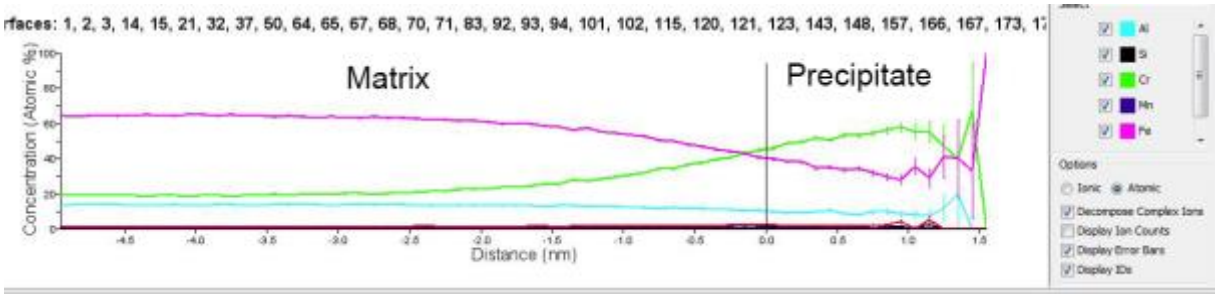

Figure 9.5. Precipitate concentration profile from aged SZ and its interface